

# Quantum Differential Equation Solver via Hybrid Oscillator-Qubit Linear Combination of Hamiltonian Simulations

Elin Ranjan Das<sup>1,2</sup>, Muqing Zheng<sup>\*2</sup>, Rishab Dutta<sup>2</sup>, Ang Li<sup>2,3</sup>, Timothy Stavenger<sup>2</sup>, and Yuan Liu<sup>†1,4,5</sup>

<sup>1</sup>Department of Electrical and Computer Engineering, North Carolina State University, Raleigh, North Carolina 27695, USA

<sup>2</sup>Pacific Northwest National Laboratory, Richland, WA, USA, 99354

<sup>3</sup>Department of Electrical and Computer Engineering, University of Washington, Seattle, WA, USA, 98195

<sup>4</sup>Department of Computer Science, North Carolina State University, Raleigh, North Carolina 27695, USA

<sup>5</sup>Department of Physics, North Carolina State University, Raleigh, North Carolina 27695, USA

## Abstract

We introduce a hybrid oscillator-qubit formulation of linear combination of Hamiltonian simulation (LCHS) for solving linear ordinary differential equations. Instead of representing the quadrature rule with a discrete-variable (DV) ancilla register in qubit-only LCHS, the method encodes the LCHS kernel in a continuous-variable (CV) ancillary mode, thereby eliminating the explicit  $\mathcal{O}(\log M_a)$  ancilla-qubit overhead, where  $M_a$  is the number of discretized integral terms in the DV quadrature rule. We derive analytical error bounds for two main approximation mechanisms for the ideal kernel state preparation, showing superalgebraic convergence for Schwartz-class kernels and subexponential convergence under stronger strip-analytic assumptions in the truncation cutoff  $N$ , where  $N$  denotes the number of squeezed-Fock basis components in the kernel-state expansion. The required CV non-Gaussianity is captured by the finite squeezed-Fock kernel state, which generically has stellar rank  $N - 1$ , identifying the truncation cutoff as a discrete measure of the oracle's non-Gaussian resource. For the hybrid oscillator-qubit evolution, we also obtain a product-formula bound showing that a  $p$ th-order formula requires  $\mathcal{O}(t^{1+1/p}(\Gamma_{p,N}/\epsilon t)^{1/p})$  Trotter steps to reach error  $\epsilon t$ , where  $\Gamma_{p,N}$  collects Pauli commutator terms weighted by powers of the truncated position-operator norm  $\|\hat{x}\|_N$ . We further derive a perturbation bound for the probability of obtaining the required oscillator measurement outcome, showing that an  $\epsilon$ -close implementation of the ideal LCHS oracle in operator norm induces only an  $\mathcal{O}(\epsilon)$  perturbation in the postselection probability. In the heat-equation benchmarks, the Law–Eberly protocol achieves end-to-end solution fidelity at least 99.90%, while the optimized 30-layer SNAP+ $\mathcal{D}$  route achieves at least 99.68%. A comparison with a matrix-product-state-based DV LCHS implementation further shows that, at matched or better solution quality, the hybrid construction uses a substantially more compact oracle description with reduce circuit cost.

## 1 Introduction

Hamiltonian simulation approximates time-evolution operators and forms the basis of many quantum algorithms, including those for solving differential equations [1]. One of the most powerful algorithmic paradigms for Hamiltonian simulation is the linear combinations of unitaries (LCU) method [2, 3, 4]. In this framework, the target Hamiltonian evolution is decomposed into a process governed by a weighted sum of time-evolution operators, enabling time evolution with provable complexity bounds. Building on this idea, a broader class of quantum algorithms has been developed for solving partial differential equations (PDEs), including approaches that reformulate PDEs as linear systems [5, 6, 7]. Within this context, Schrödingerisation [8, 9] and linear combination of Hamiltonian simulation (LCHS) [10, 11] methods provide a systematic way to construct evolution operators while maintaining controllable error scaling. However, existing implementations of LCHS rely

\*muqing.zheng@pnnl.gov

†q\_yuanliu@ncsu.edu

exclusively on discrete-variable (qubit-based) architectures, where continuous degrees of freedom must first be discretized.

Continuous-variable (CV) quantum systems such as harmonic oscillators realized in photonic modes or superconducting cavities naturally encode infinite-dimensional Hilbert spaces [12, 13]. These systems are well suited for representing bosonic modes and field-theoretic models without the need for coarse discretization [14]. Building on this, CV-based quantum algorithms for solving partial differential equations leverage the native continuous degrees of freedom to bypass the qubit overhead typically associated with high-dimensional systems [15]. Meanwhile, qubit-based platforms provide strong nonlinearity, robust control, and efficient implementation of conditional operations. Hybrid oscillator-qubit architectures combine the advantages of both paradigms, offering expanded computational expressiveness and improved resource efficiency [15, 16].

Despite their natural compatibility with continuous degrees of freedom, hybrid CV–DV architectures cannot be used for LCHS by a direct substitution of a qubit quadrature register with an oscillator mode. The formal LCHS kernel is a continuous object, whereas a physical oscillator implementation must use a normalizable, finite-energy state that can be synthesized with finite resources. Moreover, the hybrid evolution involves oscillator operators such as  $\hat{x}$ , which are unbounded on the full Hilbert space and therefore require a careful truncation-dependent error analysis. The postselected oracle also introduces several coupled approximation mechanisms: finite squeezed-Fock kernel-state truncation, imperfect oscillator-state synthesis, product-formula simulation error, and postselection normalization. Thus, the central challenge is to obtain a physically implementable oscillator encoding of the LCHS kernel while preserving rigorous control of the total algorithmic error and circuit cost.

In this work, we propose a hybrid oscillator-qubit formulation of LCHS for linear ordinary differential equations, including those obtained from spatial discretization of PDEs, in which the discrete quadrature registers are replaced by ancillary CV modes. This reformulation realizes the LCHS kernel through a joint oscillator-qubit evolution, yielding a more compact oracle and shifting the main approximation error toward the preparation of the ancillary CV states. We develop the corresponding error analysis, separating kernel-state squeezed-Fock truncation, oscillator-state synthesis, and product-formula simulation errors. We also present two circuit-level methods for preparing the truncated non-Gaussian initial oscillator state: Law–Eberly (LE) synthesis using Jaynes–Cummings (JC) pulses and qubit rotations, and a variational SNAP+ $\mathcal{D}$  approach based on displacement and selective number-dependent arbitrary phase (SNAP) gates. We validate the framework numerically on heat equations with three types of boundary conditions.

The rest of this article is organized as follows. In Section 2, we summarize our main results, highlighting the performance of our hybrid implementation against DV LCHS baselines. In Section 3, we provide the technical motivation, formally defining the LCHS kernel and the scaling limitations of current DV quadrature registers. Section 4 establishes the methodology, where we introduce the CV encoding for LCHS and derive error bounds for squeezed-Fock kernel-state truncation and Trotterized hybrid evolution, as well as the required non-Gaussianity resource through discrete (stellar rank) and continuous (quantum relative entropy) metric. In Section 5, we apply the framework to practical examples, including the damped harmonic oscillator and the one-dimensional heat equation with various boundary conditions. Section 6 describes the circuit-level realization, detailing the compilation of hybrid interactions and the use of Law–Eberly and variational synthesis for state preparation. Finally, Section 7 presents numerical experiments and a direct resource comparison with DV LCU baselines, followed by concluding remarks and future directions in Section 8. Throughout this paper, we use the  $\hbar = 2$  convention.

## 2 Summary of Main Results

For the benchmark instances, the hybrid oscillator-qubit formulation of LCHS combines analytical error control with a circuit-level oscillator-state preparation route and shows an advantage over the considered DV baselines in both oracle description size and computational resource cost while maintaining the solution quality. It offers a resource-efficient alternative in regimes where quadrature cost is dominant for differential-equation simulation, particularly when the quadrature cost of standard LCHS becomes the primary limitation. Our key findings are summarized in the following subsections.

### 2.1 Formal Hybrid LCHS Framework

We now establish the mathematical foundation of the continuous-discrete variable LCHS framework. The key result is that the non-unitary evolution generated by a linear system can be represented exactly through a larger unitary evolution acting jointly on an ancillary continuous-variable oscillator and a finite-dimensional register.

**Result 1 (Informal version of Theorem 1).** *Let  $A \in \mathbb{C}^{D \times D}$ . If  $A = L + iH$  with  $L = L^\dagger \succeq 0$  and  $H = H^\dagger$ , then the non-unitary evolution generated by  $A$  can be represented as the projection of a joint unitary evolution on*

an ancilla oscillator and the original finite-dimensional system,  $e^{-At} = (\langle \phi |_{\text{osc}} \otimes \mathbb{I}_q) e^{-it(\hat{x} \otimes L + \mathbb{I}_{\text{osc}} \otimes H)} (|\psi \rangle_{\text{osc}} \otimes \mathbb{I}_q)$ , where the oscillator states satisfy  $\phi^*(x)\psi(x) = \frac{f(x)}{1-ix} \equiv g(x)$ , where  $f(x)$  is the kernel function defined in [10, 11].

The target function  $g(x)$  derived from LCHS kernel is encoded through the overlap of a prepared initial oscillator state  $|\psi \rangle_{\text{osc}}$  and a postselected squeezed vacuum state  $\langle \phi |_{\text{osc}}$ . This mapping removes the explicit  $\mathcal{O}(\log M_a)$  ancilla-qubit overhead that DV quadrature registers require for  $M_a$  discretized integral terms, replacing it with  $\mathcal{O}(1)$  ancillary oscillators. The formulation outlines the extension to inhomogeneous systems by utilizing a second oscillator to encode the required time-window weight. The formulation has been discussed in Appendix A.6.

In practice, the oscillator state  $|\psi \rangle_{\text{osc}}$  is implemented using a normalized finite squeezed-Fock expansion, as described in Section 4.1. The key approximation result is that the truncated squeezed-Fock representation converges rapidly to the ideal kernel state.

**Result 2 (Informal version of Theorem 2).** *The finite squeezed-Fock basis approximation converges to the ideal kernel state in the  $L^2$  norm. For Schwartz-class targets, the convergence is superalgebraic in the truncation dimension  $N$ , while stronger analyticity assumptions yield subexponential convergence.*

The hybrid oscillator-qubit evolution introduces an additional approximation error associated with product-formula simulation. The resulting Trotterization cost depends on both the truncated oscillator operators and the commutator structure of the encoded generators.

**Result 3 (Informal version of Theorem 3).** *For the hybrid oscillator-qubit evolution, a  $p^{\text{th}}$  order product formula requires  $n_t = \mathcal{O}\left[t^{1+1/p} \left(\frac{\Gamma_{p,N}}{\epsilon_t}\right)^{1/p}\right]$  Trotter steps to achieve simulation error  $\epsilon_t$ . Here  $\Gamma_{p,N}$  summarizes the relevant Pauli-level commutator contributions, including mixed L-H terms weighted by powers of the truncated position-operator norm  $\|\hat{x}\|_N$ . Thus, increasing the Fock cutoff can improve the squeezed-Fock approximation while increasing the cost of controlling product-formula error.*

Because the oracle is implemented through postselection, approximation errors in the hybrid evolution also affect the success probability of the protocol. The key result is that the deviation in postselection probability can be controlled directly in terms of the total operator approximation error.

**Result 4 (Informal version of Theorem 4).** *Let  $\epsilon_{\text{tot}} := \|K_{\text{evol}}(t) - K_{\infty}(t)\|$ , where  $K_{\infty}(t)$  denotes the ideal postselected evolution operator*

$$K_{\infty}(t) := (\langle \phi_r |_{\text{osc}} \otimes \mathbb{I}_q) U_{\infty}(t) (|\psi_{\infty} \rangle_{\text{osc}} \otimes \mathbb{I}_q), \quad (1)$$

and  $K_{\text{evol}}(t)$  its implementation using finite squeezed-Fock truncation and product-formula simulation

$$K_{\text{evol}}(t) := (\langle \phi_r |_{\text{osc}} \otimes \mathbb{I}_q) U_{\text{evol}}(t) (|\psi_N \rangle_{\text{osc}} \otimes \mathbb{I}_q), \quad (2)$$

where  $U_{\infty}(t) = e^{-it(\hat{x} \otimes L + \mathbb{I}_{\text{osc}} \otimes H)}$  is the exact hybrid CV-DV evolution,  $|\psi_{\infty} \rangle_{\text{osc}}$  is the ideal kernel state,  $|\psi_N \rangle_{\text{osc}}$  its squeezed-Fock basis approximation, and  $U_{\text{evol}}(t)$  the  $n_t$ -step product-formula approximation. Then the induced change in postselection success probability is bounded by  $2\|K_{\infty}(t)\|\epsilon_{\text{tot}} + \epsilon_{\text{tot}}^2$ . Thus, approximation errors from both kernel-state truncation and product-formula simulation translate directly into sampling overhead for postselection.

## 2.2 Performance and Resource Benchmarks

We benchmark hybrid CV-DV LCHS against DV LCHS using the 100-step Trotterized heat equation with Dirichlet boundary condition. Compared with the DV LCHS construction, the hybrid CV-DV formulation reduces the ancillary-state oracle description size from the DV quadrature size  $M_{\text{DV}} = 320$  to  $n_{\text{coeff}} = 48$  Fock coefficients. In the Dirichlet benchmark, this corresponds to a reduction in the Trotter-block CNOT count from 4700 to 400, while also giving a slightly higher solution fidelity.

## 3 Background and Motivation

Consider the linear ordinary differential equation

$$\frac{du(t)}{dt} = -A(t)u(t) + b(t), \quad u(0) = u_0. \quad (3)$$

LCHS provides an efficient quantum framework for solving such linear ODEs [10, 11]. The solution can be written as

$$u(T) = \mathcal{T}e^{-\int_0^T A(s)ds}u_0 + \int_0^T \mathcal{T}e^{-\int_s^T A(s')ds'}b(s)ds, \quad (4)$$

where  $\mathcal{T}$  denotes time ordering. Writing

$$A(t) = L(t) + iH(t), \quad L(t) = L(t)^\dagger \succeq 0, \quad H(t) = H(t)^\dagger,$$

LCHS expresses the dissipative evolution as a continuous linear combination of unitary evolutions:

$$\mathcal{T}e^{-\int_0^t A(s)ds} = \int_{\mathbb{R}} g(k) \mathcal{T}e^{-i\int_0^t (kL(s)+H(s))ds} dk, \quad (5)$$

$$\int_0^t \mathcal{T}e^{-\int_s^t A(s')ds'} b(s)ds = \int_0^t \int_{\mathbb{R}} g(k) \left[ \mathcal{T}e^{-i\int_s^t (kL(s')+H(s'))ds'} \right] b(s)dkds. \quad (6)$$

The inhomogeneous contribution is treated analogously by inserting the same representation inside the Duhamel integral. The weight function is defined as  $g(k) = \frac{f(k)}{1-ik}$ , and we use the near-optimal kernel choice [11]

$$g(k) = \frac{e^{2\beta}}{2\pi(1-ik)e^{(1+ik)\beta}}, \quad \beta \in (0, 1), \quad (7)$$

where  $\beta$  controls the analyticity and decay of the kernel.

In standard LCHS, the continuous integral is truncated and discretized, producing an LCU circuit with a quadrature register of size  $\lceil \log_2(M_a) \rceil$ . For the complementary solution,

$$M_a \in \mathcal{O} \left( T \max_t \|L(t)\| \left( \log \frac{1}{\epsilon} \right)^{1+1/\beta} \right),$$

so the cost includes both this ancilla register and the corresponding multi-controlled Hamiltonian-simulation blocks [11]. Although recent constant-factor analyses improve runtime estimates [17], the discretized quadrature register remains a significant circuit-level overhead.

Motivated by continuous LCU [18, 19], we study a hybrid CV–DV version of LCHS. In this approach,  $\mathcal{O}(1)$  ancillary oscillators, together with CV state preparation and CV measurement, replace the discrete quadrature register, while the Hamiltonian simulation remains on the qubit register. This removes quadrature-discretization overhead and shifts the remaining approximation errors to CV state preparation and hybrid Hamiltonian simulation.

## 4 Methodology

We now present the formal continuous-discrete variable LCHS representation theorem. Consider the homogeneous time-independent specialization of Eq. (3),  $A(t) = A$ ,  $b(t) = 0$ , whose solution is given by  $|u(t)\rangle = e^{-At}|u_0\rangle$ .

**Theorem 1 (Continuous-discrete variable LCHS).** *Let  $A \in \mathbb{C}^{D \times D}$ ,  $t \in [0, T]$  for some  $T$ , and  $u(t) \in \mathbb{C}^D$ . Suppose that  $A$  admits a Cartesian decomposition such that*

$$A = L + iH, \quad L \equiv \frac{A + A^\dagger}{2} \succeq 0, \quad H \equiv \frac{A - A^\dagger}{2i}. \quad (8)$$

*Then the solution to Eq. (3),  $|u(t)\rangle = e^{-At}|u_0\rangle$ , admits a continuous-discrete variable LCHS representation*

$$|u(t)\rangle = (\langle \phi |_{\text{osc}} \otimes \mathbb{I}_q) e^{-it(\hat{x} \otimes L + \mathbb{I}_{\text{osc}} \otimes H)} (|\psi\rangle_{\text{osc}} \otimes |u_0\rangle_q), \quad (9)$$

*where the oscillator states  $|\psi\rangle_{\text{osc}}$  and  $|\phi\rangle_{\text{osc}}$  satisfy*

$$\phi^*(x)\psi(x) = \frac{f(x)}{1-ix} \equiv g(x),$$

*with  $f(x)$  being the LCHS kernel function defined in [10, 11].*

*Proof.* See Appendix A.1. □

The presence of the source term  $b(t) = b$  in the time-independent form of Eq. (3) requires an additional ancillary oscillator, the details of which is explored in Appendix A.6.

Recall that, under the  $\hbar = 2$  convention used throughout this paper,  $[\hat{x}, \hat{p}] = 2i$  and  $\hat{x} = \hat{a} + \hat{a}^\dagger$ . We take the position representation of the postselection state  $|\phi\rangle_{\text{osc}}$  from Theorem 1 to be a squeezed vacuum with position-space wavefunction

$$\phi_r(x) = \frac{1}{(2\pi\sigma^2)^{1/4}} \exp\left(-\frac{x^2}{4\sigma^2}\right), \quad \sigma = e^r.$$

Formally imposing  $\phi_r^*(x)\psi_r(x) = g(x)$  gives us the position representation of the initial oscillator state  $|\psi\rangle_{\text{osc}}$ ,

$$\psi_r^{\text{form}}(x) = (2\pi\sigma^2)^{1/4} g(x) \exp\left(\frac{x^2}{4\sigma^2}\right).$$

For the near-optimal LCHS kernel in Eq. (7), this finite- $r$  function is generally not square-integrable. Thus, we use  $\psi_r^{\text{form}}$  only as a formal coefficient-generation target. The physical prepared oscillator state is a normalized finite squeezed-Fock superposition. In the limit  $r \rightarrow \infty$ , the formal function approaches the normalizable ideal kernel state  $\psi_\infty(x) := \mathcal{N}g(x)$ , where  $\mathcal{N}$  is a normalization constant.

The full algorithmic circuit is shown in Fig. 1. The oscillator state preparation oracle  $U_\psi$  realizes  $|\psi\rangle_{\text{osc}}$ , the middle block implements the joint oscillator-qubit evolution, and the inverse squeezing plus vacuum postselection realizes  $\langle\phi_r|_{\text{osc}}$ . Note that the one extra ancillary qubit required by the LE protocol is not shown in the figure.

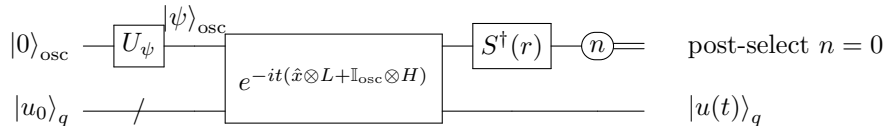


Figure 1: Algorithmic circuit for CV-DV LCHS in the homogeneous time-independent setting. The state-preparation block  $U_\psi$  loads the finite oscillator state, the middle block implements the hybrid evolution, and postselection after  $S^\dagger(r)$  projects onto the squeezed-vacuum bra  $\langle\phi_r|_{\text{osc}} = \langle 0|S^\dagger(r)$ .

## 4.1 State Preparation and Fock Truncation

This subsection specifies the oscillator state-preparation block  $U_\psi$  in Fig. 1. The limiting target state  $\psi_\infty(x) = \mathcal{N}g(x)$  is the ideal normalizable kernel state obtained from the formal construction as  $r \rightarrow \infty$ . Since infinite squeezing is not physically realizable, the implemented oracle instead prepares a normalized finite squeezed-Fock state

$$|\psi_{N,r,r',\beta}\rangle = S(r') \sum_{n=0}^{N-1} C_n |n\rangle = \sum_{n=0}^{N-1} C_n |\phi_{n,r'}\rangle,$$

where  $S(r')$  is the single-mode squeezing operator,  $r$  is the postselection squeezing parameter,  $r'$  is the preparation-basis squeezing parameter with  $r' < r$ ,  $N$  is the truncation cutoff in the Fock basis, and  $\{|n\rangle\}$  are the number (Fock) states of the harmonic oscillator. The coefficients  $\{C_n\}$  are generated by projecting the formal finite- $r$  target wavefunction  $\psi_r^{\text{form}}$  onto the squeezed Fock basis functions  $\{\phi_{n,r'}(x)\}$ . In position representation, the squeezed Fock basis functions are given by

$$\phi_{n,r'}(x) = \frac{1}{\sqrt{\sqrt{2}\sigma'}} h_n\left(\frac{x}{\sqrt{2}\sigma'}\right), \quad \sigma' = e^{r'},$$

where

$$h_n(y) = \pi^{-1/4} (2^n n!)^{-1/2} H_n(y) e^{-y^2/2}$$

is the  $n^{\text{th}}$  normalized Hermite function and  $H_n$  denotes the physicists' Hermite polynomial. Since  $\psi_r^{\text{form}}$  is generally not square-integrable for finite  $r$ , the following projection should be understood as a coefficient-generating pairing rather than as an inner product between two physical oscillator states:

$$\tilde{C}_n = \langle\phi_{n,r'}|\psi_r^{\text{form}}\rangle = \int_{\mathbb{R}} \phi_{n,r'}^*(x) \psi_r^{\text{form}}(x) dx$$

The physical coefficients are then obtained by normalization,

$$C_n = \frac{\tilde{C}_n}{\left(\sum_{m=0}^{N-1} |\tilde{C}_m|^2\right)^{1/2}}.$$

Using the explicit forms of  $\phi_{n,r'}(x)$  and  $\psi_r^{\text{form}}(x)$ , this expression reduces to

$$\tilde{C}_n = \sqrt{\frac{\sigma}{\sigma'}} \frac{1}{\sqrt{2^n n!}} \int_{\mathbb{R}} H_n\left(\frac{x}{\sqrt{2}\sigma'}\right) g(x) e^{-\gamma x^2} dx \quad (10)$$

where

$$\gamma = \frac{1}{4} \left( \frac{1}{\sigma'^2} - \frac{1}{\sigma^2} \right) = \frac{1}{4} \left( e^{-2r'} - e^{-2r} \right), \quad \sigma = e^r, \quad \sigma' = e^{r'}.$$

For the specific kernel from (7), the coefficients take the explicit form

$$\tilde{C}_n = \sqrt{\frac{\sigma}{\sigma'}} \frac{1}{\sqrt{2^n n!}} \int_{\mathbb{R}} \frac{e^{2\beta} H_n\left(\frac{x}{\sqrt{2}\sigma'}\right) e^{-\gamma x^2}}{2\pi(1-ix)e^{(1+ix)\beta}} dx, \quad (11)$$

In general, this integral does not admit a closed-form expression for arbitrary  $\beta$ . However, analytic results can be obtained for specific values of  $\beta$ . Two examples of closed analytic form for the limit values of  $\beta = \{0, 1\}$  are given in Appendix A.2. The squeezed-Fock truncation of the ideal state  $\psi_\infty$  is formalized in Theorem 2.

## 4.2 Error Bound Estimation for State Preparation

We now quantify the approximation error incurred by truncating the squeezed-Fock expansion of the ideal kernel state  $\psi_\infty(x) = \mathcal{N}g(x)$ .

In prior work [15], a sub-optimal kernel  $f(k) = \frac{1}{\pi(1+ik)}$  was realized using a single squeezed vacuum state  $\frac{1}{\sqrt{s\pi^{1/4}}} e^{-\frac{k^2}{2s^2}}$ , achieving a maximum fidelity of 98.6% at squeezing factor  $s = 0.925$ . In contrast, our construction employs a superposition of squeezed Fock states, which enables significantly improved approximation properties. As shown below, the near-optimal LCHS kernel in [11] yields a Fock-truncation error that *decays super-algebraically with the cutoff  $N$* , and under stronger assumptions, admits a *faster bound of the form  $\exp(-c\sqrt{N})$  for some constant  $c > 0$* .

The truncated state  $\psi_{N,r'}$  corresponds to the orthogonal projection of  $\psi_\infty$  onto the first  $N$  squeezed Fock basis functions. Under the change of variables  $x = \sigma'y$ , this projection is equivalent to a truncated Hermite expansion of the rescaled function

$$F_{r'}(y) = \sqrt{\sigma'} \psi_\infty(\sigma'y).$$

The approximation error, therefore, reduces to bounding the decay of Hermite coefficients of  $F_{r'}$ . The following theorem and corollary make this precise.

**Theorem 2** (Error bound for the finite squeezed-Fock truncation). *Let  $\psi_\infty(x) = \mathcal{N}g(x)$  denote the ideal normalized kernel state, where the normalization constant  $\mathcal{N}$  is chosen so that  $\|\psi_\infty\|_2 = 1$ . For a fixed squeezing parameter  $r'$ , let  $\sigma' = e^{r'}$ , and let  $\mathbb{H}_{N,r'}$  be the  $N$ -dimensional subspace spanned by the squeezed Fock basis functions  $\{\phi_{n,r'}(x)\}_{n=0}^{N-1}$ . Let  $\Pi_{N,r'}^F : L^2(\mathbb{R}) \rightarrow \mathbb{H}_{N,r'}$  denote the orthogonal projection onto this subspace, and set*

$$\psi_{N,r'} = \Pi_{N,r'}^F \psi_\infty.$$

*Let the rescaled target  $F_{r'}(y) = \sqrt{\sigma'} \psi_\infty(\sigma'y)$ . Then, the following two bounds hold.*

- (i) *Let  $\mathcal{S}$  be the Schwartz space of rapidly decaying  $C^\infty$  functions on  $\mathbb{R}$ . If  $F_{r'} \in \mathcal{S}(\mathbb{R})$ , then for every fixed integer  $s \geq 1$  and  $N \geq s$ ,*

$$\|\psi_\infty - \psi_{N,r'}\|_2 \leq \frac{\|\mathcal{A}^s F_{r'}\|_2}{\sqrt{N(N-1)\cdots(N-s+1)}}, \quad \mathcal{A} = \frac{1}{\sqrt{2}} \left( y + \frac{d}{dy} \right).$$

*Consequently, for fixed  $r'$  and every fixed  $s$ ,*

$$\|\psi_\infty - \psi_{N,r'}\|_2 = \mathcal{O}(N^{-s/2}).$$

(ii) If, in addition,  $F_{r'}$  is analytic in the strip  $|\text{Im}(y)| < \rho/\sigma'$  and there exist constants  $\mathcal{K} > 0$  and  $\sigma_0 \in \mathbb{R}$  such that  $|e^{y^2/2} F_{r'}(y)| \leq \mathcal{K}|y|^{\sigma_0}$  as  $|y| \rightarrow \infty$  within this strip, and

$$\widehat{V}_{r'} := \int_{\partial\mathcal{S}_{\rho/\sigma'}} |e^{y^2/2} F_{r'}(y)| |dy| < \infty,$$

then there is a constant  $C_{r'}$ , independent of  $N$ , such that

$$\|\psi_\infty - \psi_{N,r'}\|_2 \leq C_{r'} \exp\left(-\frac{\rho}{\sigma'} \sqrt{2(N-1)}\right).$$

In this case, for fixed  $r'$  and  $\rho$ , it is sufficient to choose

$$N = \mathcal{O}\left(e^{2r'} \log^2 \frac{1}{\epsilon_s}\right).$$

*Proof.* See appendix A.3. □

**Corollary 1** (Near-optimal LCHS kernel). *Let  $g(k) = \frac{e^{2\beta}}{2\pi(1-ik)e^{(1+ik)\beta}}$ ,  $\beta \in (0, 1)$ , be the near-optimal LCHS kernel in Eq. (7) and  $g \in \mathcal{S}(\mathbb{R})$ . Consequently, the normalized ideal kernel state  $\psi_\infty = \mathcal{N}g$  satisfies the hypothesis of Theorem 2(i). Hence, for any fixed  $r'$  and every fixed integer  $s \geq 1$ ,*

$$\|\psi_\infty - \Pi_{N,r'}^F \psi_\infty\|_2 = \mathcal{O}(N^{-s/2}).$$

*Proof.* See Appendix A.4. □

Theorem 2 and Corollary 1 provide the analytic squeezed Fock truncation guarantee for the ideal normalized kernel state  $\psi_\infty = \mathcal{N}g$ . The finite- $r$  coefficient construction used in the simulations is a regularized realization of this ideal target, that is, the coefficients are computed from  $\psi_r^{\text{form}}$  and the resulting finite squeezed-Fock state is normalized before use. The additional effects of this finite-squeezing regularization and of the chosen state-synthesis procedure are included in the numerical fidelity results reported in Section 7.

### 4.3 Non-Gaussianity and Stellar Rank of the Prepared States

Let

$$|\chi_N\rangle = \sum_{n=0}^{N-1} C_n |n\rangle \quad (12)$$

denote the normalized finite superposition of unsqueezed Fock states. The associated stellar, or Bargmann, function is

$$F_{\chi_N}(z) = \sum_{n=0}^{N-1} \frac{C_n}{\sqrt{n!}} z^n.$$

The stellar rank  $r_\star(\chi_N)$  is defined as the number of zeros of  $F_{\chi_N}(z)$ , counted with multiplicity [20]. If the highest coefficient is nonzero,  $C_{N-1} \neq 0$ , then  $F_{\chi_N}(z)$  is a polynomial of degree  $N-1$ . Hence, in the generic case,  $r_\star(\chi_N) = N-1$ . More generally,  $r_\star(\chi_N) = \max\{n : C_n \neq 0\}$ . Since  $S(r')$  is a Gaussian unitary, it preserves the stellar rank. Therefore,

$$r_\star(\psi_{N,r,r',\beta}) = r_\star(\chi_N), \quad (13)$$

which is generically  $N-1$ .

The stellar rank provides a discrete witness of non-Gaussianity: pure Gaussian states have stellar rank zero, while finite Fock superpositions with positive stellar rank are non-Gaussian. Thus, the truncation cutoff  $N$  sets the maximum stellar-rank complexity available to the implementable oracle state. In the formal limit  $N \rightarrow \infty$ , the ideal kernel state generally has infinite stellar rank, unless it reduces to a Gaussian state or to a Gaussian unitary applied to a finite superposition of Fock states.

The non-Gaussianity can also be quantified using the quantum relative-entropy (QRE) non-Gaussianity [21, 22],  $\delta_{\text{nG}}(\rho) = H(\tau_\rho) - H(\rho)$ , where  $\tau_\rho$  is the Gaussian state with the same first and second moments as  $\rho$ , and  $H(\cdot)$  is the von Neumann entropy of  $(\cdot)$ . Since the prepared state is pure and  $S(r')$  is a Gaussian unitary, this quantity can be computed from the unsqueezed core state  $|\chi_N\rangle$ :

$$\delta_{\text{nG}}(S(r') |\chi_N\rangle) = \delta_{\text{nG}}(|\chi_N\rangle).$$

Define  $\alpha = \langle a \rangle$ ,  $\bar{n} = \langle a^\dagger a \rangle$ ,  $m = \langle a^2 \rangle$ , where all expectation values are taken with respect to  $|\chi_N\rangle$ . Using  $a|n\rangle = \sqrt{n}|n-1\rangle$  and  $a^2|n+2\rangle = \sqrt{(n+1)(n+2)}|n\rangle$ , we obtain

$$\alpha = \langle \chi_N | a | \chi_N \rangle = \sum_{n=0}^{N-2} C_n^* C_{n+1} \sqrt{n+1}, \quad \bar{n} = \langle \chi_N | a^\dagger a | \chi_N \rangle = \sum_{n=0}^{N-1} n |C_n|^2,$$

$$m = \langle \chi_N | a^2 | \chi_N \rangle = \sum_{n=0}^{N-3} C_n^* C_{n+2} \sqrt{(n+1)(n+2)}.$$

The centered second moments are  $N_c = \langle \Delta a^\dagger \Delta a \rangle = \bar{n} - |\alpha|^2$ ,  $M_c = \langle (\Delta a)^2 \rangle = m - \alpha^2$ , with  $\Delta a = a - \langle a \rangle$ . The determinant of the single-mode covariance matrix is

$$\det V = \left( N_c + \frac{1}{2} \right)^2 - |M_c|^2.$$

The corresponding symplectic eigenvalue is

$$\nu = \sqrt{\det V} = \sqrt{\left( N_c + \frac{1}{2} \right)^2 - |M_c|^2}.$$

Therefore, for the pure state  $|\chi_N\rangle$  [13],

$$\delta_{\text{nG}} = \left( \nu + \frac{1}{2} \right) \ln \left( \nu + \frac{1}{2} \right) - \left( \nu - \frac{1}{2} \right) \ln \left( \nu - \frac{1}{2} \right).$$

This gives the exact relative-entropy non-Gaussianity of the prepared state in terms of the expansion coefficients  $C_n$ .

Finally, consider the middle block representing the hybrid interaction in Figure 1. The term  $\hat{x} \otimes L$  acts, in the eigenbasis of  $L$ , as

$$e^{-it(\hat{x} \otimes L)} = \sum_{\lambda \in \text{spec}(L)} e^{-it\lambda\hat{x}} \otimes |\lambda\rangle\langle\lambda|.$$

On each  $L$ -eigenvalue branch, the oscillator therefore experiences  $e^{-it\lambda\hat{x}}$ , which is a momentum-displacement Gaussian unitary. Thus, if the qubit register is prepared in an eigenstate of  $L$ , the interaction acts as a classically controlled Gaussian operation and does not increase the oscillator stellar rank.

However, if the qubit is prepared in a superposition basis (e.g., an  $X$ -basis state such as  $|+\rangle$ ), the evolution generates a coherent superposition of distinct Gaussian displacements entangled with the qubit. Such a superposition of Gaussian unitaries is not itself Gaussian, and therefore the effective operation on the oscillator (upon projection or when viewed independently) becomes non-Gaussian. In this sense, the controlled displacement is Gaussian under classical conditioning but becomes non-Gaussian when the control is in quantum superposition.

We emphasize that the resource discussed here is continuous-variable non-Gaussianity rather than discrete-variable stabilizer magic. The prepared oscillator state supplies the non-Gaussian resource, quantified discretely by the stellar rank and continuously by the relative-entropy non-Gaussianity. The hybrid interaction is Gaussian on each oscillator branch, and the final squeezed-vacuum postselection is also Gaussian; hence, these operations do not create oscillator non-Gaussianity by themselves. Instead, they convert the non-Gaussian structure of the prepared oscillator kernel state into the effective postselected operation acting on the qubit register. A separate analysis would be required to quantify discrete-variable stabilizer magic in the final qubit state.

#### 4.4 Trotter-Suzuki Approximation for Hamiltonian Evolution

This subsection bounds the product-formula approximation of the joint evolution block in Fig. 1, with the corresponding Suzuki–Trotter implementation shown schematically in Fig. 2. Since the hybrid Hamiltonian  $H_{\text{hyb}} = \hat{x} \otimes L + \mathbb{I}_{\text{osc}} \otimes H$  is not directly realizable as a native interaction, its time evolution needs to be synthesized via a Trotter-Suzuki decomposition into a sequence of implementable operations. The number of Trotter steps  $n_t$  required to reach a target precision  $\epsilon_t$  is determined by the non-commutativity across three distinct interaction levels: the outer CV–DV split, the inner Pauli decomposition of  $L$ , and the inner Pauli decomposition of  $H$ , as well as the energy constraints of the ancillary oscillator.

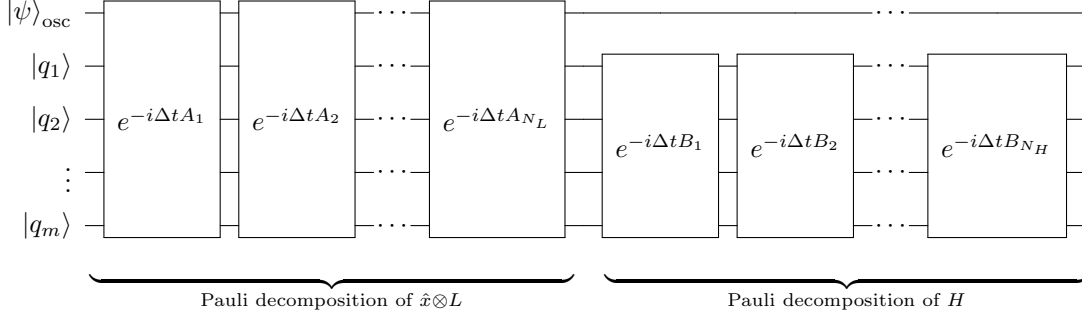


Figure 2: Schematic of a single Suzuki–Trotter layer  $S_p(\Delta t)$ , with  $\Delta t = t/n_t$ , used to approximate the hybrid evolution. The full product-formula approximation is obtained by repeating this layer  $n_t$  times.

**Theorem 3** (Resource Complexity for Hybrid Hamiltonian Evolution). *Consider the hybrid Hamiltonian  $H_{\text{hyb}} = \hat{x} \otimes L + \mathbb{I}_{\text{osc}} \otimes H$  with Pauli decompositions*

$$L = \sum_{i=1}^{N_L} \alpha_i P_i, \quad H = \sum_{j=1}^{N_H} \beta_j Q_j.$$

Let  $A_i \equiv \alpha_i \hat{x} \otimes P_i$ ,  $B_j \equiv \beta_j \mathbb{I}_{\text{osc}} \otimes Q_j$ . Define the set of implemented Hamiltonian summands  $\mathcal{G} \equiv \{A_i\}_{i=1}^{N_L} \cup \{B_j\}_{j=1}^{N_H}$ . For a  $p^{\text{th}}$ -order Suzuki–Trotter formula  $S_p(t/n_t)$ , define the mixed Pauli-level commutator sums  $\Gamma_{p,a}^{(L,H)}$  for words containing exactly a number of  $L$ -sector summands and  $(p+1-a)$   $H$ -sector summands, and define  $\Gamma_p^{(L)}$  and  $\Gamma_p^{(H)}$  for the pure inner Pauli splits of  $L$  and  $H$ :

$$\begin{aligned} \Gamma_{p,a}^{(L,H)} &\equiv \sum_{\substack{R_1, \dots, R_{p+1} \in \mathcal{G} \\ \#_L(R_1, \dots, R_{p+1}) = a \\ \#_H(R_1, \dots, R_{p+1}) = p+1-a}} \|[R_{p+1}, [R_p, \dots, [R_2, R_1] \dots]]\| \\ \Gamma_p^{(L)} &\equiv \sum_{i_1, \dots, i_{p+1}} |\alpha_{i_1} \dots \alpha_{i_{p+1}}| \|[P_{i_{p+1}}, [P_{i_p}, \dots, [P_{i_2}, P_{i_1}] \dots]]\| \\ \Gamma_p^{(H)} &\equiv \sum_{j_1, \dots, j_{p+1}} |\beta_{j_1} \dots \beta_{j_{p+1}}| \|[Q_{j_{p+1}}, [Q_{j_p}, \dots, [Q_{j_2}, Q_{j_1}] \dots]]\| \end{aligned}$$

Let  $\Pi_N = \sum_{\ell=0}^{N-1} |\ell\rangle\langle\ell|$  and define  $\|\hat{x}\|_N := \|\Pi_N \hat{x} \Pi_N\|$ . It is sufficient to choose the number of Trotter steps as

$$n_t = \mathcal{O} \left[ t^{1+1/p} \left( \frac{\sum_{a=1}^p \|\hat{x}\|_N^a \Gamma_{p,a}^{(L,H)} + \|\hat{x}\|_N^{p+1} \Gamma_p^{(L)} + \Gamma_p^{(H)}}{\epsilon_t} \right)^{1/p} \right],$$

to ensure

$$\left\| e^{-iH_{\text{hyb}}t} - \left[ S_p \left( \frac{t}{n_t} \right) \right]^{n_t} \right\| \leq \epsilon_t.$$

The corresponding gate counts scale as

$$N_{\text{CNOT}} = \mathcal{O} \left( 2n_t m_p \left[ \sum_{i=1}^{N_L} \max(w(P_i) - 1, 0) + \sum_{j=1}^{N_H} \max(w(Q_j) - 1, 0) \right] \right),$$

and

$$N_{\text{hyb}} = \mathcal{O}(n_t m_p N_L),$$

where  $m_p$  is the number of exponentials in the  $p^{\text{th}}$ -order Suzuki formula (for standard recursive Suzuki formulas,  $m_{2k} = 3 \cdot 5^{k-1}$ ),  $N_L$  and  $N_H$  are the numbers of Pauli terms in  $L$  and  $H$ , and  $w(\cdot)$  denotes Pauli weight.

*Proof.* See Appendix A.5. □

**Remark 1.** For a pure qubit Hamiltonian ( $L = 0$ ), the error scaling reduces to the commutator scaling relation for Trotterization error on qubits, since  $\Gamma_p^{(L)} = 0$  and  $\Gamma_{p,a}^{(L,H)} = 0$  for all  $a$ ,

$$n_t = \mathcal{O} \left[ t^{1+1/p} \left( \frac{\Gamma_p^{(H)}}{\epsilon_t} \right)^{1/p} \right]$$

For an oscillator-qubit coupled Hamiltonian ( $H = 0$ ), the mixed and pure- $H$  terms vanish, but the pure  $L$ -sector inner split remains:

$$n_t = \mathcal{O} \left[ t^{1+1/p} \left( \frac{\|\hat{x}\|_N^{p+1} \Gamma_p^{(L)}}{\epsilon_t} \right)^{1/p} \right].$$

Any linear parabolic PDE of the form  $u_t = -\mathcal{L}u$ , where  $\mathcal{L}$  is a real, Hermitian, positive elliptic operator admits, after spatial semi-discretization, a first-order ODE system:  $\frac{dU}{dt} = -AU$ , where  $A \in \mathbb{R}^{D \times D}$  is the discrete representation of  $\mathcal{L}$ , typically symmetric positive definite under appropriate boundary conditions. When central finite differences are used for spatial discretization,  $A$  inherits a sparse structured form reflecting the stencil of the discretized differential operator. For such ODEs, since  $A$  contains no anti-Hermitian component ( $H = 0$ ) in the Cartesian decomposition, the generic theorem reduces to the pure  $L$  inner-split term above. The Dirichlet heat-equation benchmark then uses the additional block structure of the finite-difference Laplacian to obtain the sharper first-order estimate in Eq. (15).

The approximation in the finite squeezed-Fock basis and the product-formula approximation together determine the accuracy of the implemented postselected oracle. Since the hybrid LCHS circuit is probabilistic, we next quantify how these approximation errors affect the oscillator postselection success probability.

## 4.5 Postselection Success Probability

The hybrid CV–DV LCHS oracle is a postselected operation. Therefore, in addition to the approximation error of the implemented operator, one must also account for the probability of successfully obtaining the desired oscillator measurement outcome. In the homogeneous time-independent setting, we defined the implemented postselected operator  $K_{\text{evol}}(t)$  in Eq. (2) and the ideal postselected operator  $K_{\infty}(t)$  in Eq. (1). For a normalized input state  $|u_0\rangle_q$ , the unnormalized output state is

$$|\tilde{u}_{\text{evol}}(t)\rangle_q = K_{\text{evol}}(t) |u_0\rangle_q.$$

The oscillator postselection succeeds with probability

$$p_{\text{succ}}^{(\text{evol})}(t; u_0) = \|K_{\text{evol}}(t) |u_0\rangle_q\|^2 = \langle u_0 | K_{\text{evol}}^\dagger(t) K_{\text{evol}}(t) |u_0\rangle.$$

Conditioned on successful postselection, the normalized output state is

$$|u_{\text{evol}}(t)\rangle_q = \frac{K_{\text{evol}}(t) |u_0\rangle_q}{\sqrt{p_{\text{succ}}^{(\text{evol})}(t; u_0)}}.$$

The following result gives a perturbation bound for the postselection success probability under operator-norm errors in the implemented LCHS oracle.

**Theorem 4** (Perturbation bound for postselection success probability). *Let  $K_{\infty}(t)$  be the ideal postselected operator,  $K_{\infty}(t) := (\langle \phi_r |_{\text{osc}} \otimes \mathbb{I}_q) U_{\infty}(t) (|\psi_{\infty}\rangle_{\text{osc}} \otimes \mathbb{I}_q)$ , and  $K_{\text{evol}}(t)$  its implementation using finite squeezed-Fock truncation and product-formula simulation,  $K_{\text{evol}}(t) := (\langle \phi_r |_{\text{osc}} \otimes \mathbb{I}_q) U_{\text{evol}}(t) (|\psi_N\rangle_{\text{osc}} \otimes \mathbb{I}_q)$ , where  $U_{\infty}(t) = e^{-it(\hat{x} \otimes L + \mathbb{I}_{\text{osc}} \otimes H)}$  is the exact hybrid CV–DV evolution,  $|\psi_{\infty}\rangle_{\text{osc}}$  is the ideal kernel state,  $|\psi_N\rangle_{\text{osc}}$  its squeezed-Fock basis approximation, and  $U_{\text{evol}}(t)$  the  $n_t$ -step product-formula approximation. Suppose*

$$\|K_{\text{evol}}(t) - K_{\infty}(t)\| \leq \epsilon_{\text{tot}}.$$

Then, for any normalized input state  $|u_0\rangle_q$ ,

$$\left| p_{\text{succ}}^{(\text{evol})}(t; u_0) - p_{\text{succ}}^{(\infty)}(t; u_0) \right| \leq 2\|K_{\infty}(t)\| \epsilon_{\text{tot}} + \epsilon_{\text{tot}}^2.$$

In particular, if  $\|K_{\infty}(t)\| \leq 1$ , then

$$\left| p_{\text{succ}}^{(\text{evol})}(t; u_0) - p_{\text{succ}}^{(\infty)}(t; u_0) \right| \leq 2\epsilon_{\text{tot}} + \epsilon_{\text{tot}}^2.$$

*Proof.* Let  $E(t) = K_{\text{evol}}(t) - K_{\infty}(t)$ . Then

$$K_{\text{evol}}(t) |u_0\rangle = K_{\infty}(t) |u_0\rangle + E(t) |u_0\rangle.$$

Therefore,

$$p_{\text{succ}}^{(\text{evol})} - p_{\text{succ}}^{(\infty)} = \|K_{\infty} |u_0\rangle + E |u_0\rangle\|^2 - \|K_{\infty} |u_0\rangle\|^2 = 2\text{Re} \langle K_{\infty} u_0 | E u_0 \rangle + \|E |u_0\rangle\|^2.$$

Taking absolute values and applying the Cauchy–Schwarz inequality gives

$$\left| p_{\text{succ}}^{(\text{evol})} - p_{\text{succ}}^{(\infty)} \right| \leq 2 \|K_{\infty} |u_0\rangle\| \|E |u_0\rangle\| + \|E |u_0\rangle\|^2 \leq 2 \|K_{\infty}\| \|E\| + \|E\|^2. \quad (14)$$

Using  $\|E\| \leq \epsilon_{\text{tot}}$  gives

$$\left| p_{\text{succ}}^{(\text{evol})} - p_{\text{succ}}^{(\infty)} \right| \leq 2 \|K_{\infty}(t)\| \epsilon_{\text{tot}} + \epsilon_{\text{tot}}^2.$$

If  $\|K_{\infty}(t)\| \leq 1$ , the simplified bound follows immediately.  $\square$

The total approximation error  $\epsilon_{\text{tot}}$  may include contributions from finite truncation in the squeezed-Fock basis, oscillator-state synthesis, and product-formula simulation. For example, if

$$\epsilon_{\text{tot}} \leq \epsilon_N + \epsilon_{\text{synth}} + \epsilon_t(n_t),$$

where  $\epsilon_N$  is the truncation error,  $\epsilon_{\text{synth}}$  is the oscillator-state synthesis error, and  $\epsilon_t(n_t)$  is the product-formula error after  $n_t$  Trotter steps, then Theorem 4 implies

$$\left| p_{\text{succ}}^{(\text{evol})}(t; u_0) - p_{\text{succ}}^{(\infty)}(t; u_0) \right| \leq 2 \|K_{\infty}(t)\| (\epsilon_N + \epsilon_{\text{synth}} + \epsilon_t(n_t)) + (\epsilon_N + \epsilon_{\text{synth}} + \epsilon_t(n_t))^2.$$

Thus, the postselection probability converges with the same asymptotic dependence as the implemented oracle. In particular, if the truncated kernel-state error satisfies  $\epsilon_N = \mathcal{O}(N^{-s/2})$ , then the truncated Fock basis contribution to the success-probability error also scales as  $\mathcal{O}(N^{-s/2})$ . Under the stronger strip-analytic assumptions leading to  $\epsilon_N = \mathcal{O}(e^{-c\sqrt{N}})$ , the corresponding contribution to the success-probability error likewise scales as  $\mathcal{O}(e^{-c\sqrt{N}})$ . Here  $\epsilon_{\text{synth}}$  denotes the oscillator-state synthesis error, defined as the distance between the target finite squeezed-Fock state  $|\psi_N\rangle$  and the state actually prepared by the circuit. For ideal Law–Eberly synthesis, this error is zero within the chosen truncated subspace, up to numerical precision, whereas for the variational SNAP+ $D$  route it is determined by the achieved preparation fidelity.

This bound shows that the success probability inherits the same finite cutoff dependence as the kernel-state approximation. Thus, increasing  $N$  not only improves the implemented LCHS kernel but also reduces the bound on the cutoff-induced perturbation to the postselection probability. However, increasing  $N$  can also increase the cost of Hamiltonian simulation through the truncated position-operator norm appearing in the product-formula bound. The cutoff  $N$  therefore controls a tradeoff between kernel accuracy, postselection stability, and simulation cost. This probability should be counted separately from the gate complexity and state-preparation complexity. The solution fidelities reported in the numerical benchmarks are conditioned on successful postselection, while  $p_{\text{succ}}^{(\text{evol})}$  quantifies the sampling overhead required to obtain the accepted outcomes.

The remaining implementation-dependent component is the basis-gate synthesis of the hybrid evolutions generated by  $L$  and  $H$ . This step depends strongly on the structure of the matrices and is therefore problem-specific. Many previous works in the DV regime tackle this problem by decomposing coefficient matrices into linear combinations of Pauli matrices, for example, hyperbolic partial differential equations [23] and advection-diffusion equation [24]. Borrowing their designs and following the circuit synthesis in [19], the evolution of decomposed Hamiltonians coupled with oscillators can be constructed in CV–DV circuits. With the general hybrid CV–DV LCHS framework in place, we now consider several representative ODE and PDE examples and develop the corresponding  $L$  and  $H$  oracle constructions in each case in the next section.

## 5 Simulating linear ODE and PDE examples

### 5.1 Example: Damped Harmonic Oscillator

Consider a damped harmonic oscillator with position  $x(t)$ , damping rate  $\zeta \geq 0$ , and angular frequency  $\omega > 0$  and the underdamped condition  $\omega^2 - \zeta^2/4 > 0$ . Its equation of motion is

$$\frac{d^2x}{dt^2} + \zeta \frac{dx}{dt} + \omega^2 x = 0.$$

Introducing a new constant  $\kappa := \sqrt{\omega^2 - \zeta^2/4}$  and a new variable  $v := \frac{1}{\kappa}(\dot{x} + \frac{\zeta}{2}x)$ , this second-order equation can be written as a first-order linear system

$$\frac{d}{dt} \begin{bmatrix} x \\ v \end{bmatrix} = - \begin{bmatrix} \zeta/2 & -\kappa \\ \kappa & \zeta/2 \end{bmatrix} \begin{bmatrix} x \\ v \end{bmatrix}.$$

We denote the coefficient matrix by  $A$ .

To cast the dynamics into the LCHS framework, we perform the Cartesian decomposition of  $A$ ,

$$L = \frac{A + A^\dagger}{2} = \frac{\zeta}{2}I \succeq 0, \quad H = \frac{A - A^\dagger}{2i} = -\kappa Y,$$

where  $I$  is the identity matrix and  $Y$  is the Pauli- $Y$  matrix. Since  $L \propto I$ , the two terms commute, and therefore

$$e^{-it(kL+H)} = e^{-itkL}e^{-itH}.$$

The corresponding unitary operators appearing in the LCHS circuit construction are therefore

$$\exp(-itkL) = \exp\left(-iI\frac{\zeta tk}{2}\right), \quad \exp(-itH) = \exp(i\kappa tY).$$

Thus, the dissipative contribution associated with  $L = \frac{\zeta}{2}I$  is encoded in each LCHS branch as the  $k$ -dependent phase  $e^{-i(\zeta tk/2)}$ , while the Hamiltonian contribution generates the qubit rotation  $e^{i\kappa tY}$ . The physical damping factor is recovered only after the CV-weighted integral and postselection.

## 5.2 Example: Heat Equation

### 5.2.1 One-dimensional Dirichlet Case

Consider the one-dimensional heat equation

$$\frac{\partial u(x, t)}{\partial t} = \alpha \frac{\partial^2 u(x, t)}{\partial x^2}, \quad 0 < x < \mathcal{L},$$

with initial condition  $u(x, 0) = u_0(x)$  and homogeneous Dirichlet boundary conditions  $u(0, t) = u(\mathcal{L}, t) = 0$ . Without loss of generality, let  $m$  be the number of qubits in the DV register, and assume that  $M = 2^m$  is the number of interior grid points, let  $h = \mathcal{L}/(M + 1)$ , and write  $u_j(t) = u(x_j, t)$  for the interior values. The second-order central difference approximation gives the ODE

$$\frac{d}{dt}u(t) = -A_m^{(D)}u(t), \quad A_m^{(D)} := \frac{\alpha}{h^2}T_m^{(D)},$$

where  $u(t) = (u_1(t), \dots, u_M(t))^\top$  and the Dirichlet Laplacian is

$$T_m^{(D)} = 2I^{\otimes m} - \sum_{x=0}^{M-2} (|x\rangle\langle x+1| + |x+1\rangle\langle x|).$$

We order the qubits from least to most significant as  $q_0, \dots, q_{m-1}$ . For  $m = 2$ ,

$$T_2^{(D)} := \begin{bmatrix} 2 & -1 & 0 & 0 \\ -1 & 2 & -1 & 0 \\ 0 & -1 & 2 & -1 \\ 0 & 0 & -1 & 2 \end{bmatrix} = 2I_1 I_0 - I_1 X_0 - \frac{1}{2}(X_1 X_0 + Y_1 Y_0).$$

Since  $A_m^{(D)}$  is real symmetric, its Cartesian decomposition satisfies  $L = A_m^{(D)}$  and  $H = \mathbf{0}$ . Therefore one hybrid CV-DV product-formula step takes the form

$$\mathcal{U}_m^{(D)}(\delta t) := \exp\left(-i\theta \hat{x} \otimes T_m^{(D)}\right), \quad \theta := \frac{\alpha \delta t}{h^2},$$

where  $\delta t = t/n_t$  for  $n_t$  product-formula steps over total runtime  $t$ .

The Dirichlet Laplacian admits the decomposition

$$T_m^{(D)} = 2I^{\otimes m} - \sum_{c=0}^{m-1} R_c, \quad R_c = \sigma_c^+ \prod_{j=0}^{c-1} \sigma_j^- + \sigma_c^- \prod_{j=0}^{c-1} \sigma_j^+,$$

with  $\sigma_j^\pm := \frac{X_j \mp iY_j}{2}$ . The first few terms are  $R_0 = X_0$  and  $R_1 = \frac{1}{2}(X_1X_0 + Y_1Y_0)$ , thus,  $T_2^{(D)} = 2I_0I_1 - R_0 - R_1$ . Using a first-order product formula, one Trotter step is compiled as

$$\mathcal{U}_m^{(D)}(\delta t) \approx e^{-i2\theta \hat{x} \otimes I^{\otimes m}} \prod_{c=0}^{m-1} e^{i\theta \hat{x} \otimes R_c}.$$

Since  $A_m^{(D)}$  is real symmetric, the only product-formula error comes from the inner compilation of  $T_m^{(D)}$  into the blocks  $\{2I^{\otimes m}, R_0, \dots, R_{m-1}\}$ . The identity block commutes with every  $R_c$ , so only distinct pairs  $R_c$  and  $R_{c'}$  contribute.

$$[\hat{x} \otimes R_c, \hat{x} \otimes R_{c'}] = \hat{x}^2 \otimes [R_c, R_{c'}],$$

Because  $\|R_c\| = 1$ , each commutator obeys  $\|[R_c, R_{c'}]\| \leq 2$ , and there are  $\binom{m}{2} = \mathcal{O}(\log^2 M)$  such pairs. Accumulating over  $n_t$  product-formula steps with  $\delta t = t/n_t$  therefore gives

$$\epsilon_{\text{tot,heat}} = \mathcal{O}\left(\frac{t^2}{n_t} \frac{\alpha^2}{\hbar^4} \|\hat{x}\|_N^2 \log^2 M\right). \quad (15)$$

The step count  $n_t$  is then chosen so that  $\epsilon_{\text{tot,heat}}$  stays below the desired tolerance. Each  $R_c$  contains  $2^c$  Pauli strings with coefficients  $\pm 2^{-c}$ ,

$$R_c = 2^{-c} \sum_{\ell=1}^{2^c} s_{c,\ell} P_{c,\ell}, \quad s_{c,\ell} \in \{\pm 1\},$$

where each  $P_{c,\ell}$  has support on  $q_0, \dots, q_c$  and an even number of  $Y$  operators. Hence any two  $P_{c,\ell}$  differ on an even number of qubits and commute, so

$$e^{i\theta \hat{x} \otimes R_c} = \prod_{\ell=1}^{2^c} e^{i\theta 2^{-c} s_{c,\ell} \hat{x} \otimes P_{c,\ell}}.$$

Each factor  $e^{i\theta 2^{-c} s_{c,\ell} \hat{x} \otimes P_{c,\ell}}$  is implemented by basis changes, a parity CNOT ladder on the support of  $P_{c,\ell}$ , one hybrid interaction, and uncomputation. A representative hybrid Pauli block is shown in Fig. 3.

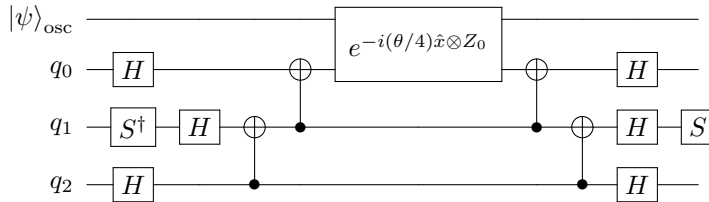


Figure 3: Compilation of the hybrid Pauli factor  $e^{-i(\theta/4)\hat{x} \otimes X_2Y_1X_0}$ . Basis changes map  $X_2Y_1X_0$  to  $Z_2Z_1Z_0$ , a CNOT ladder collects the parity on  $q_0$ , the oscillator couples through  $e^{-i(\theta/4)\hat{x} \otimes Z_0}$ , and the circuit is then uncomputed. The block  $e^{i\theta \hat{x} \otimes R_2}$  is obtained by concatenating the four commuting Pauli factors in  $R_2$ .

### 5.2.2 Other One-dimensional Boundary Conditions

Both remaining boundary conditions are obtained from the Dirichlet block by adding correction terms. For periodic boundary conditions, we have  $T_m^{(P)} = T_m^{(D)} - T_m^{\text{corr},(P)}$ , where  $T_m^{\text{corr},(P)} := |0\rangle\langle M-1| + |M-1\rangle\langle 0|$ . The Pauli decomposition of the correction term is

$$T_m^{\text{corr},(P)} = |0^m\rangle\langle 1^m| + |1^m\rangle\langle 0^m| = \prod_{j=0}^{m-1} \sigma_j^+ + \prod_{j=0}^{m-1} \sigma_j^- = 2^{1-m} \sum_{\substack{S \subseteq \{0, \dots, m-1\} \\ |S| \text{ even}}} (-1)^{|S|/2} \left( \prod_{j \notin S} X_j \right) \left( \prod_{j \in S} Y_j \right).$$

Thus  $T_m^{\text{corr},(P)}$  contributes  $2^{m-1}$  commuting Pauli strings, each of weight  $m$ .

For homogeneous Neumann boundary conditions, we have  $T_m^{(N)} = T_m^{(D)} - T_m^{\text{corr},(N)}$ , where  $T_m^{\text{corr},(N)} := |0\rangle\langle 0| + |M-1\rangle\langle M-1|$ . Similar to the periodic boundary conditions,

$$T_m^{\text{corr},(N)} = |0^m\rangle\langle 0^m| + |1^m\rangle\langle 1^m| = 2^{1-m} \sum_{\substack{S \subseteq \{0, \dots, m-1\} \\ |S| \text{ even}}} \left( \prod_{j \in S} Z_j \right) \left( \prod_{j \notin S} I_j \right).$$

Hence  $T_m^{\text{corr},(N)}$  contributes  $2^{m-1}$  commuting  $Z$ -type strings, one of which is the identity. In both cases one reuses  $\mathcal{U}_m^{(bc)}(\delta t) := \exp(-i\theta \hat{x} \otimes T_m^{(bc)})$ . The boundary condition changes the Pauli list, but not the hybrid Trotterization pattern.

### 5.2.3 $d$ -dimensional Extension

Let  $\Omega = \prod_{i=1}^d (0, L_i)$  and consider the  $d$ -dimensional heat equation

$$\frac{\partial u(\mathbf{x}, t)}{\partial t} = \alpha \sum_{i=1}^d \frac{\partial^2 u(\mathbf{x}, t)}{\partial x_i^2}, \quad \mathbf{x} \in \Omega,$$

with separable homogeneous boundary conditions  $bc_i \in \{D, P, N\}$  along each axis. Let the  $i^{\text{th}}$  coordinate be discretized with  $M_i = 2^{m_i}$  grid points and spacing  $h_i$ , and denote by  $I_{m_i} = I^{\otimes m_i}$  the identity on the corresponding coordinate subregister. The semidiscrete operator is the Kronecker sum

$$A_d^{(\mathbf{bc})} = \alpha \sum_{i=1}^d \frac{1}{h_i^2} \left( I_{m_1} \otimes \dots \otimes I_{m_{i-1}} \otimes T_{m_i}^{(bc_i)} \otimes I_{m_{i+1}} \otimes \dots \otimes I_{m_d} \right),$$

where  $\mathbf{bc} = (bc_1, \dots, bc_d)$ . The coordinate blocks commute because they act on disjoint qubit subregisters. Hence

$$\begin{aligned} \mathcal{U}_d^{(\mathbf{bc})}(\delta t) &:= \exp(-i\delta t \hat{x} \otimes A_d^{(\mathbf{bc})}) \\ &= \prod_{i=1}^d \exp\left[-i\theta_i \hat{x} \otimes \left( I_{m_1} \otimes \dots \otimes I_{m_{i-1}} \otimes T_{m_i}^{(bc_i)} \otimes I_{m_{i+1}} \otimes \dots \otimes I_{m_d} \right)\right], \end{aligned}$$

with  $\theta_i = \alpha\delta t/h_i^2$ . Each factor is compiled by the corresponding one-dimensional block.

We summarize exact gate counts of trotter blocks in Table 1, with details provided in Appendix A.7.

Table 1: Gate counts for the  $d$ -dimensional heat-equation compilation after  $n_t$  first-order product-formula steps, assuming the same boundary condition on each axis. Here  $M_i = 2^{m_i}$  is the grid size along axis  $i$ . Details are provided in Appendix A.7.

Boundary condition	Hybrid gates	CNOT gates	1-qubit gates
Dirichlet	$n_t \sum_{i=1}^d M_i$	$n_t \sum_{i=1}^d [2(m_i - 2)M_i + 4]$	$n_t \sum_{i=1}^d [3(m_i - 1)M_i + 2]$
Periodic	$n_t \sum_{i=1}^d \frac{3}{4}M_i$	$n_t \sum_{i=1}^d \left[ \left( \frac{3}{2}m_i - \frac{7}{2} \right) M_i + 4 \right]$	$n \sum_{i=1}^d \left[ \begin{cases} 6, & m_i = 2, \\ 2 + \left( \frac{9}{4}m_i - \frac{13}{4} \right) M_i, & m_i \geq 3 \end{cases} \right]$
Neumann	$n_t \sum_{i=1}^d \left( \frac{3}{2}M_i - 1 \right)$	$n_t \sum_{i=1}^d \left[ \left( \frac{5}{2}m_i - 5 \right) M_i + 6 \right]$	$n_t \sum_{i=1}^d [3(m_i - 1)M_i + 2]$

## 6 Circuit-Level Realization

In this section we describe the circuit-level realization used in our numerical study of the time-independent homogeneous CV–DV LCHS map introduced in Section 2.1. Writing  $A = L + iH$  with  $L \succeq 0$ , the implemented qubit-space map for runtime  $T$  is  $K(T)$  defined in Eq. (2). In practice,  $U_{\text{evol}}(T)$  in Eq. (2) is synthesized by a product-formula approximation as discussed in Section 4.4.

### 6.1 CV State Preparation

The truncated Fock coefficients  $\{C_n\}_{n=0}^{N-1}$  are obtained by evaluating the integral in Eq. (11) numerically via Gaussian quadrature, using the near-optimal kernel  $g(k)$  defined in Section 3. Under the  $\hbar = 2$  convention adopted throughout this paper, the Gaussian damping factor in that integral is  $\gamma = \frac{1}{4}(e^{-2r'} - e^{-2r})$  with squeezing widths  $\sigma = e^r$  and  $\sigma' = e^{r'}$ . The corresponding oscillator state  $|\psi_{\text{finite}}\rangle = |\chi_N\rangle$  (Eq. (12)) can then be synthesized in two ways.

**Law–Eberly protocol.** This scheme uses the deterministic oscillator-state synthesis procedure of Law and Eberly [25], later implemented in a superconducting resonator by Hofheinz *et al.* [26]. The target of this step is the state  $|\psi_{\text{finite}}\rangle$  prepared jointly with a two-level system in its ground state. The LE construction alternates two qubit–oscillator primitives. The first is a Jaynes–Cummings exchange pulse on the adjacent manifold  $\{|e, n-1\rangle, |g, n\rangle\}$ ,

$$S_n(\alpha, \phi) = \exp\left[-i\frac{\alpha}{\sqrt{n}}(e^{i\phi}\sigma_- a^\dagger + e^{-i\phi}\sigma_+ a)\right], \quad n \geq 1, \quad (16)$$

where the  $1/\sqrt{n}$  factor compensates the oscillator matrix element. In the present Bosonic Qiskit (version 15.1) circuit implementation, this pulse is emitted as a `cv_jc` gate. The second is the qubit rotation,

$$R_n(\theta, \varphi) = \mathbb{I}_{\text{osc}} \otimes \exp\left[-\frac{i\theta}{2}(\cos\varphi X + \sin\varphi Y)\right], \quad (17)$$

which is a standard Qiskit `r` gate on the LE ancillary qubit.

The synthesis is obtained by solving the time-reversed problem as suggested in [25]. Starting from  $|g\rangle|\psi_{\text{finite}}\rangle$ , one eliminates amplitudes from the highest occupied Fock level downward. For  $n = N-1, \dots, 1$ , a JC pulse  $S_n$  is chosen to eliminate the amplitude on  $|g, n\rangle$ , rotating it into the excited state  $|e, n-1\rangle$ . A qubit rotation  $R_{n-1}$  then removes the resulting amplitude on  $|e, n-1\rangle$ . After the recursion, the state has been mapped to  $|g, 0\rangle$  up to an irrelevant global phase. The preparation circuit is the adjoint of this unpreparation sequence, applied in reverse order, as summarized in Algorithm 1.

---

**Algorithm 1** Law–Eberly synthesis used for the CV state preparation oracle

---

**Require:** Normalized coefficients  $\{C_n\}_{n=0}^{N-1}$

**Ensure:** Gate list preparing  $|\psi_{\text{finite}}\rangle$

- 1: Set the symbolic reverse state  $|\Psi_{\text{rev}}\rangle \leftarrow |g\rangle \sum_{n=0}^{N-1} C_n |n\rangle$
  - 2: Set  $\mathcal{P}_{\text{unprep}} \leftarrow []$
  - 3: **for**  $n = N-1, N-2, \dots, 1$  **do**
  - 4:     Set  $a_n = \langle e, n-1 | \Psi_{\text{rev}} \rangle$  and  $b_n = \langle g, n | \Psi_{\text{rev}} \rangle$
  - 5:     **if**  $|b_n| > 0$  **then** ▷ Choose  $S_n$  so that the updated amplitude on  $|g, n\rangle$  is zero.
  - 6:         **if**  $|a_n| = 0$  **then**
  - 7:             Set  $\alpha_n = \pi/2$  and  $\phi_n = 0$
  - 8:         **else**
  - 9:             Set  $\alpha_n = \arctan(|b_n|/|a_n|)$  and  $\phi_n = \arg b_n - \arg a_n - \pi/2$
  - 10:         **end if**
  - 11:          $|\Psi_{\text{rev}}\rangle \leftarrow S_n(\alpha_n, \phi_n) |\Psi_{\text{rev}}\rangle$
  - 12:         Append  $S_n(\alpha_n, \phi_n)$  to  $\mathcal{P}_{\text{unprep}}$
  - 13:     **end if**
  - 14:     Set  $u_{n-1} = \langle e, n-1 | \Psi_{\text{rev}} \rangle$  and  $v_{n-1} = \langle g, n-1 | \Psi_{\text{rev}} \rangle$
  - 15:     **if**  $|u_{n-1}| > 0$  **then** ▷ Choose  $R_{n-1}$  so that the updated amplitude on  $|e, n-1\rangle$  is zero.
  - 16:         **if**  $|v_{n-1}| = 0$  **then**
  - 17:             Set  $\theta_{n-1} = \pi$  and  $\varphi_{n-1} = 0$
  - 18:         **else**
  - 19:             Set  $\theta_{n-1} = 2 \arctan(|u_{n-1}|/|v_{n-1}|)$  and  $\varphi_{n-1} = -\arg u_{n-1} + \arg v_{n-1} + \pi/2$
  - 20:         **end if**
  - 21:          $|\Psi_{\text{rev}}\rangle \leftarrow R_{n-1}(\theta_{n-1}, \varphi_{n-1}) |\Psi_{\text{rev}}\rangle$
  - 22:         Append  $R_{n-1}(\theta_{n-1}, \varphi_{n-1})$  to  $\mathcal{P}_{\text{unprep}}$
  - 23:     **end if**
  - 24: **end for**
  - 25: Return  $\mathcal{P}_{\text{prep}} = (\mathcal{P}_{\text{unprep}})^\dagger$  in reverse order
- 

The circuit-level realization of the returned preparation sequence is shown in Fig. 4. For a target with support on all  $N$  levels, this produces  $N-1$  JC pulses and  $N-1$  qubit rotations. Thus, for the numerical experiments with  $N = 48$  in Section 7, the ideal LE realization reports 47 JC pulses and 47 qubit rotations.

**Variational SNAP-plus-displacement (SNAP+D) synthesis.** Another implementation uses universal oscillator control generated by selective number-dependent arbitrary phase (SNAP) gates together with dis-

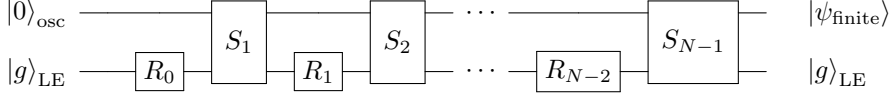


Figure 4: Circuit-level Law–Eberly state preparation of the finite oscillator seed state. Each  $R_n$  block is a standard `r` gate in Qiskit and each  $S_n$  block is emitted as a `cv_jc` gate.

placements [27, 28]. In this picture, we seek a variational approximation of the form

$$U_{\text{SNAP}+\mathcal{D}} = \prod_{\ell=1}^{N_{\text{layer}}} [\mathcal{D}(\alpha_\ell) \text{SNAP}(\boldsymbol{\theta}_\ell)],$$

where  $N_{\text{layer}}$  is a user-defined parameter for the number of  $\text{SNAP}+\mathcal{D}$  layers and  $\text{SNAP}(\boldsymbol{\theta}_\ell) = \sum_{n=0}^{N-1} e^{i\theta_{\ell,n}} |n\rangle\langle n|$ . The variational parameters are optimized to maximize the state-preparation fidelity,

$$\max_{\{\alpha_\ell, \boldsymbol{\theta}_\ell\}} |\langle \psi_{\text{finite}} | U_{\text{SNAP}+\mathcal{D}} | 0 \rangle|^2.$$

This route is implemented directly at the circuit level in Bosonic Qiskit [29, 30] using `cv_snap` and `cv_d` gates. Prior works have numerically shown that optimized  $\text{SNAP}+\mathcal{D}$  sequences can prepare oscillator states with high fidelity at relatively short depth [31, 32]. Also, the excellent expressiveness of the  $\text{SNAP}+\mathcal{D}$  ansatz has been recently corroborated on non-trivial electronic ground states from quantum chemistry [33].

## 6.2 Gate-level Compilation of Hybrid Evolution

Built upon Section 4.4, the compiled evolution consists of hybrid factors  $e^{-i\Delta t \alpha_i \hat{x} \otimes P_i}$  and qubit-only factors  $e^{-i\Delta t \beta_j Q_j}$ . The latter are standard DV Pauli rotations, so the only new CV–DV implementation ingredient is the compilation of a single hybrid factor  $e^{-i\Delta t c_m \hat{x} \otimes P_m}$ . Each Pauli term is compiled by a basis change  $B_m$  that diagonalizes  $P_m$  into the  $Z$  basis, followed by a parity mapping  $C_m$  onto a target qubit  $t$ :

$$e^{-i\Delta t c_m \hat{x} \otimes P_m} = B_m^\dagger C_m^\dagger e^{-i\Delta t c_m \hat{x} \otimes Z_t} C_m B_m.$$

The primitive hybrid interaction admits the conditional-displacement form

$$c\mathcal{D}(-i\lambda) = e^{-i\lambda \hat{x} \otimes Z_t} = \mathcal{D}(-i\lambda) \otimes |0\rangle\langle 0|_t + \mathcal{D}(i\lambda) \otimes |1\rangle\langle 1|_t,$$

where  $\mathcal{D}(\alpha) = e^{\alpha a^\dagger - \alpha^* a}$  and, under the  $\hbar = 2$  convention,  $e^{-i\lambda \hat{x}} = \mathcal{D}(-i\lambda)$ .

## 7 Numerical Experiments

We study the one-dimensional heat equation with Dirichlet, Neumann, and periodic boundary conditions on a two-qubit register. The implementations in this section are based on Bosonic Qiskit (version 15.1) [29, 30]. Unless stated otherwise, the target is the exact discretized solution  $u(T) = e^{-AT}u(0)$  at  $T = 1$ , with oscillator truncation  $n_{\text{Fock}} = 64$  and first-order Trotterization with  $n_t = 100$  steps. The numerical study uses a four-dimensional semidiscrete system with  $M = 4$ ,  $\alpha = 1$ ,  $h = 1$ ,  $T = 1$ , and initial state  $u(0) = |01\rangle$ . Since  $\alpha/h^2 = 1$  in all three cases, the semidiscrete generators are

$$\begin{aligned} T_2^{(D)} &= 2I_1 I_0 - I_1 X_0 - \frac{1}{2}(X_1 X_0 + Y_1 Y_0), \\ T_2^{(N)} &= \frac{3}{2}I_1 I_0 - I_1 X_0 - \frac{1}{2}(X_1 X_0 + Y_1 Y_0 + Z_1 Z_0), \\ T_2^{(P)} &= 2I_1 I_0 - I_1 X_0 - X_1 X_0. \end{aligned}$$

Note that  $T_2^{(P)}$  has the least number of Pauli terms and does not contain relatively costly Pauli  $Y$ , as Pauli  $Y$  need both RZ and H gates for basis change. Consequently,  $T_2^{(P)}$  has lower gate counts in the trotter block compared to the other two coefficient matrices. For normalized states, fidelities are reported as

$$F(\psi, \phi) = |\langle \psi | \phi \rangle|^2$$

and the exact target solution vector is  $u_{\text{exact}}(T) = e^{-AT}u(0)$ . We use

$$F_{\text{LE}} = F(u_{\text{LE}}, u_{\text{exact}}), \quad F_{\text{SNAP}} = F(u_{\text{SNAP}}, u_{\text{exact}})$$

where  $u_{\text{LE}}$  and  $u_{\text{SNAP}}$  are the DV solution vectors produced by the CV–DV LCHS circuit after postselection using the circuit-level LE and SNAP+ $\mathcal{D}$  CV state-preparation routes, respectively. The LE route deterministically prepares the target truncated oscillator state in the ideal qubit–oscillator circuit model, while SNAP+ $\mathcal{D}$  gives a variational approximation. Thus  $F_{\text{LE}}$  and  $F_{\text{SNAP}}$  report the corresponding end-to-end PDE fidelities. The quantity  $n_{\text{coeff}}$  denotes the number of oscillator Fock amplitudes in the truncated CV oracle state.

## 7.1 Parameter Selection and Optimal Fidelities

During the parameter sweeps, ideal CV state injection, a simulator-only method that directly initializes the truncated oscillator state, is used for state preparation to avoid state-preparation error. We select the kernel parameters  $r$ ,  $r'$ , and  $\beta$  for sweeps. The overall search domain covered

$$r \in [1.92, 8.40], \quad r' \in [0.975, 4.50], \quad \beta \in [0.3, 0.9],$$

with  $n_{\text{coeff}} \in \{24, 48\}$  and  $n_t = 100$ . The highest-fidelity region was then sampled more densely on the intervals  $r \in [7.8, 8.4]$  and  $r' \in [4.0, 4.5]$ , which is the domain represented in Fig. 5. For each displayed value of a given parameter, the plotted point is the best exact fidelity obtained while that parameter is held fixed and the remaining parameters vary over the tested grid. Across all three boundary conditions, the oracle-baseline optima lie in a narrow high-squeezing region. Dirichlet is optimized at  $(r, r', \beta, n_{\text{coeff}}) = (7.9, 4.1, 0.5, 48)$ , Neumann at  $(7.9, 4.0, 0.3, 48)$ , and periodic at  $(8.1, 4.1, 0.3, 48)$ .

In those sweeps, increasing the oscillator cutoff from  $n_{\text{coeff}} = 24$  to 48 improves the best infidelity in all three cases: from  $4.32 \times 10^{-3}$  to  $1.04 \times 10^{-3}$  for Dirichlet, from  $4.40 \times 10^{-4}$  to  $2.85 \times 10^{-4}$  for Neumann, and from  $7.04 \times 10^{-4}$  to  $2.75 \times 10^{-4}$  for periodic. This is consistent with the truncation-error bounds derived in Theorem 2 that larger truncated oscillator resources improve the approximation.

The best points in the same sweep also place the optimum in a large-squeezing regime, with  $r$  around 8 and  $r'$  around 4. In the CV–DV LCHS construction, the ancillary oscillator appears through the matrix element  $\langle \phi | e^{-it(\hat{x} \otimes L + I \otimes H)} | \psi \rangle$ , so the oscillator is the degree of freedom whose position-quadrature amplitudes supply the continuous LCHS weights. Larger values of  $r$  and  $r'$  therefore indicate that the prepared and postselected oscillator states must be sufficiently spread in quadrature space to reproduce the required kernel profile for the target evolution operator  $A = L + iH$ .

The optimized 30-layer SNAP+ $\mathcal{D}$  circuits achieve CV-state-preparation infidelity at most 0.562% among the three boundary conditions (specifically, 0.562% for Dirichlet, 0.495% for Neumann, 0.314% for periodic). To see the resulting end-to-end PDE solution infidelities, Table 2 compares circuit-level LE and SNAP+ $\mathcal{D}$  methods at the selected parameter choices. For all three boundary conditions, the optimized SNAP+ $\mathcal{D}$  circuit achieves a similar level of end-to-end infidelity as the ideal LE route, while LE prepares the target truncated CV state deterministically in the ideal circuit model.

Table 2: Selected parameter choices, non-Gaussianity diagnostics, corresponding infidelities  $1 - F_{\text{LE}}$  and  $1 - F_{\text{SNAP}}$ , and postselection probabilities. In all three cases,  $n_{\text{coeff}}$  is set to 48 and SNAP+ $\mathcal{D}$  experiments use 30 ansatz layers.

Boundary	$r$	$r'$	$\beta$	$n_{\text{coeff}}$	$\delta_{\text{nG,LE}}$	$1 - F_{\text{LE}}$	$p_{\text{post,LE}}$	$\delta_{\text{nG,SNAP}}$	$1 - F_{\text{SNAP}}$	$p_{\text{post,SNAP}}$
Dirichlet	7.9	4.1	0.5	48	2.22	$1.04 \times 10^{-3}$	6.28%	1.78	$3.18 \times 10^{-3}$	6.27%
Neumann	7.9	4.0	0.3	48	1.98	$2.84 \times 10^{-4}$	5.62%	1.45	$3.22 \times 10^{-4}$	5.49%
Periodic	8.1	4.1	0.3	48	2.01	$2.75 \times 10^{-4}$	4.84%	1.67	$4.69 \times 10^{-4}$	4.78%

In addition to the end-to-end fidelities mentioned above, at the circuit level, our numerical experiments indicate that the main practical discrepancy in the SNAP+ $\mathcal{D}$  rows comes from preparing the ancillary CV oracle state rather than from the subsequent hybrid evolution. To show this point, we look at  $F(u_{\text{SNAP}}, u_{\text{trunc}})$  where  $u_{\text{trunc}}$  is the ideal output predicted by the truncated CV–DV model when the actually prepared ancillary CV state is used as input. Thus this comparison isolates the hybrid-evolution error after state preparation. In the 30-layer SNAP+ $\mathcal{D}$  runs, the associated infidelity is less than  $1.6 \times 10^{-5}$  in all three boundary conditions. By contrast, the CV-state preparation infidelities from these SNAP+ $\mathcal{D}$  ansatzes are  $5.62 \times 10^{-3}$  for Dirichlet,  $4.95 \times 10^{-3}$  for Neumann, and  $3.14 \times 10^{-3}$  for periodic. This shows that, once the ancillary CV state has been prepared, the remaining hybrid evolution is already much more accurate.

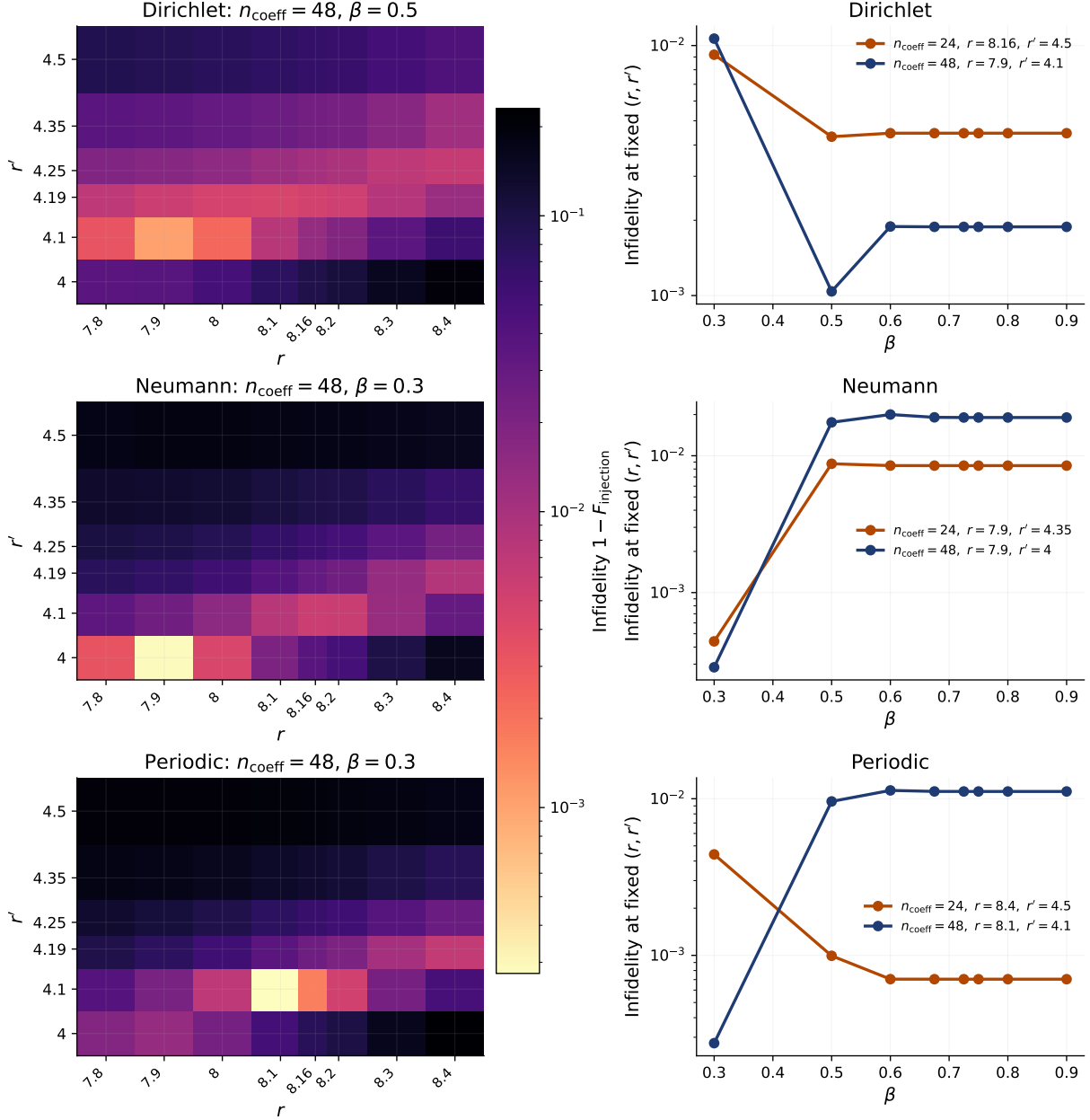


Figure 5: Infidelity sensitivity under ideal CV state injection in the refined parameter domain  $r \in [7.8, 8.4]$ ,  $r' \in [4.0, 4.5]$ , and  $\beta \in [0.30, 0.90]$  for three boundary conditions. The left column shows  $1 - F_{\text{injection}}$  over  $(r, r')$  at  $n_{\text{coeff}} = 48$  with  $\beta = 0.5$  for Dirichlet and  $\beta = 0.3$  for Neumann and periodic. The right column shows  $1 - F_{\text{injection}}$  versus  $\beta$  at fixed  $(r, r')$  under  $n_{\text{coeff}} \in \{24, 48\}$ .  $F_{\text{injection}} = F(u_{\text{injection}}, u_{\text{exact}})$ , where  $u_{\text{injection}}$  is the DV solution vector produced by the CV–DV LCHS circuit after postselection using ideal state injection for CV state preparation.

## 7.2 Resource Costs

All experiments used a qumode with  $N_{\text{Fock}} = 64$  (emulated by 6 qubits in Bosonic Qiskit) and 2 qubits for hybrid qumode-qubit Hamiltonian simulation, with 1 extra ancillary qubit when the CV state-preparation method is Law–Eberly synthesis.

Law–Eberly synthesis provides an exact circuit-level state synthesis baseline together with JC and qubit rotation counts. For all three boundary conditions, the LE circuit matches the ideal state-loading baseline to numerical precision and reports 47 JC pulses and 47 qubit rotations.

For the hybrid evolution block, the 100-step Trotterized CV–DV evolution uses qubit basis-change gates, CNOT ladders, unconditional displacements, and qubit-controlled displacements. The 1Q column aggregates the DV basis-change  $H$  and  $R_Z$  gates. The two outer squeezing gates contribute a fixed Gaussian overhead, SNAP+ $\mathcal{D}$  contributes the non-Gaussian oracle-preparation cost, and LE contributes the qubit-assisted JC

and qubit rotation sequence. Here one  $\text{SNAP}_{48} + \mathcal{D}$  layer means a SNAP gate with 48 active number-state phases followed by one unconditional displacement operation. Ideal direct state loading is used only for kernel-parameter selection and is not counted as a synthesis primitive. The overall gate counts are reported in Table 3 and verify derivations in Section A.7 at  $m = 2$ .

It is also worth noting that the coefficient matrix for the periodic boundary condition,  $A^{(P)}$ , only contains 2 non-identity Pauli terms and no Pauli  $Y$  matrix contribution. This significantly reduces gate counts in the Trotter block, although  $A^{(P)}$  has more non-zero matrix entries than  $A^{(D)}$ .

Table 3: Resource counts for the circuit-level LE baseline and for the SNAP+ $\mathcal{D}$  circuits in Table 2. The Trotter columns refer only to the 100-step hybrid evolution block: aggregated single-qubit DV gates, CNOTs, unconditional CV displacements ( $\mathcal{D}$ ), and controlled displacements ( $c\mathcal{D}$ ). The two outer squeezing gates are excluded. The SNAP+ $\mathcal{D}$  column gives the number of  $\text{SNAP}_{48} + \mathcal{D}$  layers used in the non-Gaussian oracle preparation stage.

Boundary	Optimizer	SNAP+ $\mathcal{D}$	Law–Eberly			Trotter Block			
	Iterations	Layers	JC pulses	R gate	Ancillary qubit	1Q gates	CNOTs	$\mathcal{D}$	$c\mathcal{D}$
Dirichlet	62	30	47	47	1	1400	400	100	300
Neumann	64	30	47	47	1	1400	600	100	400
Periodic	67	30	47	47	1	600	200	100	200

### 7.3 Comparison with DV LCHS

For the DV LCHS baseline, the first question is the size of the quadrature discretization. In the homogeneous heat-equation benchmark considered here,  $H = 0$  and  $L = A^{(bc)}$ , where  $bc$  corresponds to three boundary conditions, so the standard DV LCHS formulas in [10, 11] give

$$h_1 = \frac{1}{\epsilon T \|L\|_2}, \quad K = \eta \left\lceil \frac{(\log(1/\epsilon))^{1/\beta}}{h_1} \right\rceil, \quad Q = \left\lceil \frac{1}{\log 4} \log \left( \frac{8}{3C_\beta} \frac{K}{\epsilon} \right) \right\rceil,$$

$$C_\beta = 2\pi e^{-2^\beta}, \quad M_{\text{DV}} = 2 \left\lceil \frac{K}{h_1} \right\rceil Q, \quad m_c = \lceil \log_2 M_{\text{DV}} \rceil.$$

Here  $h_1$  is the quadrature step size,  $K$  is the truncation half-width of the  $k$  interval,  $Q$  is the Gauss–Legendre order on each subinterval,  $M_{\text{DV}}$  is the number of resulting LCU terms, and  $m_c$  is the control-register width. In Table 4, we fix  $\eta = 1$  and  $\epsilon = 0.1$  and report parameter values. For each boundary condition, we then choose the value of  $\beta$  from the scan  $\beta \in [0.60, 1)$  that maximizes the classical DV fidelity  $F_{\text{DV}} = F(u_{\text{DV}}, u_{\text{exact}})$ , where  $u_{\text{DV}}$  is the classical DV LCHS output for the same initial state.

Table 4: Optimal DV LCHS quadrature parameters from the classical  $\beta$  scan with  $\epsilon = 0.1$  and  $\eta = 1$ . The last two columns report the resulting classical solution infidelity  $1 - F_{\text{DV}}$  and the fidelity gap  $F_{\text{LE}} - F_{\text{DV}}$  relative to the Law–Eberly baseline.

Boundary	$\beta_{\text{opt}}$	$h_1$	$K$	$Q$	$M_{\text{DV}}$	$m_c$	$\ c\ _1$	$1 - F_{\text{DV}}$	$F_{\text{LE}} - F_{\text{DV}}$
Dirichlet	0.60	0.10168	4.06718	4	320	9	0.9357	$2.33 \times 10^{-3}$	$1.30 \times 10^{-3}$
Neumann	0.90	0.10775	2.58599	4	192	8	1.2073	$2.26 \times 10^{-3}$	$1.98 \times 10^{-3}$
Periodic	0.80	0.09197	2.85107	4	248	8	1.0740	$2.78 \times 10^{-4}$	$3.00 \times 10^{-6}$

The DV method requires 320, 192, and 248 quadrature terms for Dirichlet, Neumann, and periodic boundary conditions (corresponding to 9, 8, and 8 ancillary qubits, respectively), whereas our CV–DV example uses  $n_{\text{coeff}} = 48$  Fock coefficients and 64 Fock levels in each case. The corresponding factors between  $M_{\text{DV}}$  and  $n_{\text{coeff}}$  are approximately 6.67, 4.00, and 5.17. In fidelity, the circuit-level LE baseline is higher than the best classical DV solution by  $1.30 \times 10^{-3}$  for Dirichlet and  $1.98 \times 10^{-3}$  for Neumann, while the periodic case is essentially matched, with a difference of only  $3.00 \times 10^{-6}$ .

For circuit-level comparison, on the DV side, the ancilla amplitude vector can be compressed as a matrix product state (MPS), so ancilla preparation need not scale like generic amplitude loading. For the Dirichlet benchmark, the practical DV circuit considered here uses a nine-qubit control register and applies the ancilla preparation and unpreparation only once, while repeating the controlled LCHS evolution block:

$$\langle 0_{\text{anc}} | U_{\text{prep}}^\dagger [U_{\text{ctrl}}(T/n)]^n U_{\text{prep}} | 0_{\text{anc}} \rangle, \quad n = 100, \quad T = 1.$$

As summarized in Table 5, in this implementation, the ancilla preparation block uses 130 one-qubit gates and 48 CNOT gates, while a single controlled-evolution slice uses 53 one-qubit gates and 47 CNOT gates. Repeating the evolution block for 100 slices, with prepare (PREP) operator and the uncomputation of PREP, yields a total circuit depth of 9227, with 5561 one-qubit gates and 4796 CNOT gates. By comparison, the Dirichlet CV–DV implementation uses 1400 single-qubit gates, 400 CNOTs, 100  $\mathcal{D}$ , and 300  $c\mathcal{D}$  in the Trotterized middle block, together with a 30-layer SNAP+ $\mathcal{D}$  preparation routine. Thus, for this benchmark, the repeated DV qubit circuit has substantially larger DV gate depth and CNOT count even after MPS compression of the ancilla state, whereas the CV–DV implementation shifts part of the oracle cost into oscillator operations such as SNAP, displacement, squeezing, and controlled displacement.

Table 5: Operator counts for the Dirichlet DV LCHS circuit in the form of 9 control qubits, an MPS-compressed ancilla state, and  $n = 100$  repeated controlled-evolution slices.

Block	Depth	1Q gates	CNOT
Ancilla PREP	71	130	48
Controlled Evolution	9100	5300	4700
Full circuit	9227	5561	4796

## 8 Conclusion and Future Work

We introduced a hybrid oscillator-qubit formulation of LCHS for linear differential equations, replacing the quadrature qubits of standard DV LCHS with a qumode. In this formulation, the LCHS integral is realized through a qumode sandwich acting on a joint oscillator-qubit evolution. We derived analytical error bounds for ideal kernel-state squeezed-Fock truncation and product-formula simulation, and gave a gate-level compilation in terms of Gaussian CV operations, controlled displacements, and standard qubit Pauli compilation. We used the one-dimensional heat equation as the main benchmark for the analytical and circuit-level construction.

The analytical bounds separate the main approximation mechanisms. For the oscillator state, Theorem 2 and Corollary 1 show that the Fock truncation error for the near-optimal LCHS kernel in [11] decays faster than any fixed algebraic power of the Fock cutoff. Under stronger strip-analytic assumptions, the same Hermite-expansion analysis gives a faster bound of the form  $\exp(-c\sqrt{N})$  for some constant  $c > 0$ . These results support using a normalized finite squeezed Fock superposition to approximate the ideal normalized kernel state.

For the hybrid evolution, the product-formula bound gives a sufficient number of Trotter steps to approximate the coupled oscillator-qubit evolution to a target precision. The estimate separates three sources of noncommutativity: mixed commutators between the oscillator-coupled dissipative terms and the qubit Hamiltonian terms, pure commutators among the dissipative Pauli terms, and pure commutators among the Hamiltonian Pauli terms. The oscillator contribution enters through the truncated position-operator norm, so increasing the Fock cutoff reduces state-truncation error but can increase the cost of controlling product-formula error. This gives the tradeoff between oscillator truncation and Trotterization in the CV–DV construction. The postselection analysis further shows that the same total operator error controls the perturbation of the success probability. Thus, the analytical error budget also bounds the overhead required to obtain accepted postselected samples.

For the one-dimensional heat equation with Dirichlet, Neumann, and periodic boundary conditions, CV–DV LCHS achieves exact-solution fidelities above 99.6% in all three cases with either Law–Eberly or SNAP+ $\mathcal{D}$  CV state preparation. The numerical trends are consistent with the truncation analysis, namely, increasing the Fock cutoff improves the approximation quality.

The comparison with DV LCHS further supports CV–DV LCHS as a practical alternative when the quadrature cost of DV LCHS is the dominant limitation. In the classical DV quadrature construction with  $\epsilon = 0.1$  and  $\eta = 1$ , the best fidelities in the scanned range correspond to solution infidelities of  $2.33 \times 10^{-3}$ ,  $2.26 \times 10^{-3}$ , and  $2.78 \times 10^{-4}$  for Dirichlet, Neumann, and periodic boundary conditions, respectively. The LE baseline is higher in fidelity for Dirichlet and Neumann and matched for periodic. At the same time, the corresponding DV quadrature constructions require  $M_{DV} = 320$ , 192, and 248 terms, whereas the CV experiments use  $n_{\text{coeff}} = 48$ . Thus, even at comparable solution quality, the CV formulation provides a substantially more compact oracle description. For the Dirichlet benchmark, the corresponding repeated DV circuit also remains deeper than the CV–DV realization.

The present numerical study uses an ideal circuit-level model and does not include oscillator loss, dephasing, thermal noise, leakage, finite measurement efficiency, or calibration error in the JC, SNAP,  $\mathcal{D}$ , and  $c\mathcal{D}$  primitives. These effects are especially important for our CV–DV algorithm because the oscillator carries the LCHS kernel state and participates in the hybrid evolution. Future work should therefore combine the resource analysis

here with noise-aware CV simulations and logical-oscillator encodings, including oscillator-into-oscillators and continuous-variable error-correction approaches [34, 35].

Extensions to advection-diffusion, nonlinear PDEs through Carleman linearization, and inhomogeneous systems remain promising directions, but their practical advantage will depend on noise, state-synthesis overhead, and problem-specific oracle structure. Overall, these results position hybrid CV–DV LCHS as a promising alternative to qubit-only formulations when quadrature complexity dominates resource costs.

## Author Contributions

ERD, MZ, RD, AL, and YL contributed to conceptualization. ERD, MZ, RD, and YL contributed to methodology. ERD, MZ, and TS contributed to software. ERD, MZ, and YL contributed to validation and formal analysis. ERD and MZ contributed to investigation and resources. MZ contributed to data curation and visualization. ERD, MZ, RD, AL, TS, and YL contributed to writing the original draft. TS and YL contributed to supervision and project administration. YL contributed to funding acquisition.

## Acknowledgments

ERD acknowledges fruitful discussions with Kaustubh Chandramouli. ERD, MZ, AL, TS, and YL acknowledge the support by the U.S. Department of Energy, Office of Science, Advanced Scientific Computing Research, under contract number DE-SC0025384. MZ and RD acknowledge support from Pacific Northwest National Laboratory’s Quantum Algorithms and Architecture for Domain Science (QuAADS) Laboratory Directed Research and Development (LDRD) Initiative. RD also acknowledges support from the U.S. Department of Energy, Office of Science, National Quantum Information Science Research Centers, Quantum Science Center (under FWP 76213) at Pacific Northwest National Laboratory. The Pacific Northwest National Laboratory is operated by Battelle for the U.S. Department of Energy under Contract No. DE-AC05-76RL01830. This research used resources of the National Energy Research Scientific Computing Center (NERSC), a Department of Energy User Facility using NERSC award ASCR-ERCAP0037555.

## Competing Interests

All authors declare no financial or non-financial competing interests.

## Data and Code Availability

All data and scripts are available in the GitHub repository [36].

## References

- [1] Dominic W. Berry, Andrew M. Childs, and Robin Kothari. Hamiltonian simulation with nearly optimal dependence on all parameters. In *2015 IEEE 56th Annual Symposium on Foundations of Computer Science*, page 792–809. IEEE, October 2015.
- [2] Andrew M. Childs and Nathan Wiebe. Hamiltonian simulation using linear combinations of unitary operations. *Quantum Info. Comput.*, 12(11–12):901–924, November 2012.
- [3] Dominic W. Berry, Andrew M. Childs, Richard Cleve, Robin Kothari, and Rolando D. Somma. Simulating hamiltonian dynamics with a truncated taylor series. *Physical Review Letters*, 114(9), March 2015.
- [4] Dominic W. Berry, Andrew M. Childs, Richard Cleve, Robin Kothari, and Rolando D. Somma. Exponential improvement in precision for simulating sparse hamiltonians. In *Proceedings of the forty-sixth annual ACM symposium on Theory of computing*, STOC ’14, page 283–292. ACM, May 2014.
- [5] Ashley Montanaro and Sam Pallister. Quantum algorithms and the finite element method. *Physical Review A*, 93(3), March 2016.
- [6] Andrew M. Childs, Jin-Peng Liu, and Aaron Ostrander. High-precision quantum algorithms for partial differential equations. *Quantum*, 5:574, November 2021.

- [7] Jin-Peng Liu, Herman Øie Kolden, Hari K. Krovi, Nuno F. Loureiro, Konstantina Trivisa, and Andrew M. Childs. Efficient quantum algorithm for dissipative nonlinear differential equations. *Proceedings of the National Academy of Sciences*, 118(35):e2026805118, 2021.
- [8] Shi Jin, Nana Liu, and Yue Yu. Quantum simulation of partial differential equations via schrödingerization. *Physical Review Letters*, 133(23), December 2024.
- [9] Shi Jin, Nana Liu, and Chuwen Ma. On schrödingerization-based quantum algorithms for linear dynamical systems with inhomogeneous terms, 2025.
- [10] Dong An, Jin-Peng Liu, and Lin Lin. Linear combination of hamiltonian simulation for nonunitary dynamics with optimal state preparation cost. *Physical Review Letters*, 131(15):150603, 2023.
- [11] Dong An, Andrew M Childs, and Lin Lin. Quantum algorithm for linear non-unitary dynamics with near-optimal dependence on all parameters: D. an, am childs, l. lin. *Communications in Mathematical Physics*, 407(1):19, 2026.
- [12] Samuel L. Braunstein and Peter van Loock. Quantum information with continuous variables. *Reviews of Modern Physics*, 77(2):513–577, June 2005.
- [13] Christian Weedbrook, Stefano Pirandola, Raúl García-Patrón, Nicolas J. Cerf, Timothy C. Ralph, Jeffrey H. Shapiro, and Seth Lloyd. Gaussian quantum information. *Reviews of Modern Physics*, 84(2):621–669, May 2012.
- [14] Kevin Marshall, Raphael Pooser, George Siopsis, and Christian Weedbrook. Quantum simulation of quantum field theory using continuous variables. *Physical Review A*, 92(6), December 2015.
- [15] Shi Jin and Nana Liu. Analog quantum simulation of partial differential equations. *Quantum Science and Technology*, 9(3):035047, June 2024.
- [16] Yuan Liu, Shraddha Singh, Kevin C. Smith, Eleanor Crane, John M. Martyn, Alec Eickbusch, Alexander Schuckert, Richard D. Li, Jasmine Sinanan-Singh, Micheline B. Soley, Takahiro Tsunoda, Isaac L. Chuang, Nathan Wiebe, and Steven M. Girvin. Hybrid oscillator-qubit quantum processors: Instruction set architectures, abstract machine models, and applications. *PRX Quantum*, 7:010201, Jan 2026.
- [17] Matthew Pocrnic, Peter D Johnson, Amara Katarbarwa, and Nathan Wiebe. Constant-factor improvements in quantum algorithms for linear differential equations. *arXiv preprint arXiv:2506.20760*, 2025.
- [18] Shantanav Chakraborty. Implementing any Linear Combination of Unitaries on Intermediate-term Quantum Computers. *Quantum*, 8:1496, October 2024.
- [19] Luke Bell, Yan Wang, Kevin C Smith, Yuan Liu, Eugene Dumitrescu, and SM Girvin. Co-designing spectral transformation oracles with hybrid oscillator-qubit quantum processors: From algorithms to compilation. *PRX Quantum*, 6(4):040359, 2025.
- [20] Ulysse Chabaud, Damian Markham, and Frédéric Grosshans. Stellar representation of non-gaussian quantum states. *Physical Review Letters*, 124(6), February 2020.
- [21] Marco G. Genoni, Matteo G. A. Paris, and Konrad Banaszek. Quantifying the non-gaussian character of a quantum state by quantum relative entropy. *Phys. Rev. A*, 78:060303(R), Dec 2008.
- [22] Marco G. Genoni and Matteo G. A. Paris. Quantifying non-gaussianity for quantum information. *Physical Review A*, 82(5), November 2010.
- [23] Yuki Sato, Ruho Kondo, Ikko Hamamura, Tamiya Onodera, and Naoki Yamamoto. Hamiltonian simulation for hyperbolic partial differential equations by scalable quantum circuits. *Phys. Rev. Res.*, 6:033246, Sep 2024.
- [24] Hiran Alipanah, Feng Zhang, Yong-Xin Yao, Richard Thompson, Nam Nguyen, Junyu Liu, Peyman Givi, Brian J McDermott, and Juan José Mendoza-Arenas. Quantum dynamics simulation of the advection-diffusion equation. *Physical Review Research*, 7(4):043318, 2025.
- [25] Chi K Law and Joseph H Eberly. Arbitrary control of a quantum electromagnetic field. *Physical review letters*, 76(7):1055, 1996.

- [26] Max Hofheinz, H Wang, Markus Ansmann, Radoslaw C Bialczak, Erik Lucero, Matthew Neeley, AD O’connell, Daniel Sank, J Wenner, John M Martinis, et al. Synthesizing arbitrary quantum states in a superconducting resonator. *Nature*, 459(7246):546–549, 2009.
- [27] Reinier W Heeres, Brian Vlastakis, Eric Holland, Stefan Krastanov, Victor V Albert, Luigi Frunzio, Liang Jiang, and Robert J Schoelkopf. Cavity state manipulation using photon-number selective phase gates. *Physical review letters*, 115(13):137002, 2015.
- [28] Stefan Krastanov, Victor V. Albert, Chao Shen, Chang-Ling Zou, Reinier W. Heeres, Brian Vlastakis, Robert J. Schoelkopf, and Liang Jiang. Universal control of an oscillator with dispersive coupling to a qubit. *Phys. Rev. A*, 92:040303, Oct 2015.
- [29] Timothy J Stavenger, Eleanor Crane, Kevin C Smith, Christopher T Kang, Steven M Girvin, and Nathan Wiebe. C2qa - bosonic qiskit. In *2022 IEEE High Performance Extreme Computing Conference (HPEC)*, pages 1–8, 2022.
- [30] Timothy J. Stavenger, Eleanor Crane, Kevin C. Smith, Christopher T. Kang, Steven M. Girvin, Nathan Wiebe, et al. Bosonic-Qiskit: Extension of Qiskit to support hybrid boson-qubit simulations. <https://github.com/C2QA/bosonic-qiskit>, 2022. C2QA project.
- [31] Thomas Fösel, Stefan Krastanov, Florian Marquardt, and Liang Jiang. Efficient cavity control with snap gates. *arXiv preprint arXiv:2004.14256*, 2020.
- [32] Marina Kudra, Mikael Kervinen, Ingrid Strandberg, Shah Nawaz Ahmed, Marco Scigliuzzo, Amr Osman, Daniel Pérez Lozano, Mats O. Tholén, Riccardo Borgani, David B. Haviland, Giulia Ferrini, Jonas Bylander, Anton Frisk Kockum, Fernando Quijandría, Per Delsing, and Simone Gasparinetti. Robust preparation of wigner-negative states with optimized snap-displacement sequences. *PRX Quantum*, 3:030301, Jul 2022.
- [33] Rishab Dutta, Nam P Vu, Chuzhi Xu, Delmar GA Cabral, Ningyi Lyu, Alexander V Soudackov, Xiaohan Dan, Haote Li, Chen Wang, and Victor S Batista. Simulating electronic structure on bosonic quantum computers. *J. Chem. Theory Comput.*, 21(5):2281–2300, 2025.
- [34] Kyungjoo Noh, S. M. Girvin, and Liang Jiang. Encoding an oscillator into many oscillators. *Phys. Rev. Lett.*, 125:080503, Aug 2020.
- [35] Fucheng Guo, Frank Mueller, and Yuan Liu. Concatenated dual displacement code for continuous-variable quantum error correction. *Phys. Rev. Res.*, pages –, Apr 2026.
- [36] Muqing Zheng. CV-DV-LCHS. <https://github.com/Firepanda415/CV-DV-LCHS>, 2026.
- [37] Christian Lubich. *From quantum to classical molecular dynamics: reduced models and numerical analysis*, volume 12. European Mathematical Society Zürich, 2008.
- [38] Haiyong Wang and Lun Zhang. Convergence analysis of hermite approximations for analytic functions, 2025.
- [39] Andrew M. Childs, Yuan Su, Minh C. Tran, Nathan Wiebe, and Shuchen Zhu. Theory of trotter error with commutator scaling. *Physical Review X*, 11(1), February 2021.

## A Appendix

### A.1 Proof of Theorem 1

Since  $A = L + iH$ , the solution of the initial-value problem is

$$|u(t)\rangle = e^{-At} |u_0\rangle = e^{-t(L+iH)} |u_0\rangle.$$

By the LCHS representation, the non-unitary evolution generated by  $L + iH$  can be written as

$$e^{-t(L+iH)} = \int_{\mathbb{R}} g(x) e^{-it(xL+H)} dx,$$

Now expand the oscillator states in the position basis:

$$|\psi\rangle_{\text{osc}} = \int_{\mathbb{R}} \psi(x) |x\rangle dx, \quad \langle\phi|_{\text{osc}} = \int_{\mathbb{R}} \phi^*(x) \langle x| dx.$$

The position operator has the spectral decomposition

$$\hat{x} = \int_{\mathbb{R}} x |x\rangle \langle x| dx.$$

Therefore, for any qubit-register state  $|v\rangle$ ,

$$(\hat{x} \otimes L + \mathbb{I}_{\text{osc}} \otimes H) (|x\rangle \otimes |v\rangle) = |x\rangle \otimes (xL + H) |v\rangle.$$

Thus the joint Hamiltonian is diagonal with respect to the oscillator position basis. Hence, by functional calculus,

$$e^{-it(\hat{x} \otimes L + \mathbb{I}_{\text{osc}} \otimes H)} (|x\rangle \otimes |v\rangle) = |x\rangle \otimes e^{-it(xL + H)} |v\rangle.$$

Applying this identity to the input state gives

$$e^{-it(\hat{x} \otimes L + \mathbb{I}_{\text{osc}} \otimes H)} (|\psi\rangle_{\text{osc}} \otimes |u_0\rangle_q) = \int_{\mathbb{R}} \psi(x) |x\rangle \otimes e^{-it(xL + H)} |u_0\rangle_q dx.$$

Now project the oscillator register onto  $\langle \phi |_{\text{osc}}$ . Using  $\langle x' | x \rangle = \delta(x' - x)$ , we obtain a continuous LCU [19] formulation for our problem,

$$(\langle \phi |_{\text{osc}} \otimes \mathbb{I}_q) e^{-it(\hat{x} \otimes L + \mathbb{I}_{\text{osc}} \otimes H)} (|\psi\rangle_{\text{osc}} \otimes |u_0\rangle_q) = \int_{\mathbb{R}} \phi^*(x) \psi(x) e^{-it(xL + H)} |u_0\rangle_q dx.$$

By assumption, the oscillator wavefunctions satisfy  $\phi^*(x)\psi(x) = g(x)$ . Therefore,

$$\begin{aligned} (\langle \phi |_{\text{osc}} \otimes \mathbb{I}_q) e^{-it(\hat{x} \otimes L + \mathbb{I}_{\text{osc}} \otimes H)} (|\psi\rangle_{\text{osc}} \otimes |u_0\rangle_q) &= \int_{\mathbb{R}} \frac{f(x)}{1 - ix} e^{-it(xL + H)} |u_0\rangle_q dx \\ &= e^{-t(L + iH)} |u_0\rangle_q = e^{-At} |u_0\rangle_q = |u(t)\rangle. \end{aligned}$$

Hence,

$$|u(t)\rangle = (\langle \phi |_{\text{osc}} \otimes \mathbb{I}_q) e^{-it(\hat{x} \otimes L + \mathbb{I}_{\text{osc}} \otimes H)} (|\psi\rangle_{\text{osc}} \otimes |u_0\rangle_q),$$

which proves the claimed continuous-discrete variable LCHS representation.

## A.2 Analytical Values of the Expansion Coefficients $C_n$ at Limit Values of $\beta$

The coefficients are defined by the projection of the signal  $g(x)$  onto the squeezed Hermite basis in the  $\hbar = 2$  convention:

$$C_n(\beta) = \mathcal{K}_n \int_{-\infty}^{\infty} \frac{H_n(x/(\sqrt{2}\sigma')) e^{-\gamma x^2}}{2\pi e^{-2\beta} e^{(1+ix)^\beta} (1-ix)} dx \quad (18)$$

where  $\mathcal{K}_n = \sqrt{\frac{\sigma}{\sigma'}} \frac{1}{\sqrt{2^n n!}}$  and  $\gamma = \frac{1}{4}(\sigma'^{-2} - \sigma^{-2})$ . We denote the coefficient functions at the limit points as  $C_n^{(0)}$  and  $C_n^{(1)}$ , corresponding to the limits  $\beta = 0$  and  $\beta = 1$ , respectively.

We employ an explicit polynomial decomposition of the Hermite-Lorentzian kernel. By defining a residual quotient polynomial

$$Q_{n-1}(x) = \frac{H_n(x/(\sqrt{2}\sigma')) - H_n(-i/(\sqrt{2}\sigma'))}{x + i},$$

we isolate the singular contribution of the complex pole at  $x = -i$ .

At the limit  $\beta = 0$ , the denominator simplifies to a standard complex Lorentzian. The exact closed-form expression is:

$$C_n^{(0)} = \mathcal{K}_n \left[ \frac{1}{2} H_n \left( -\frac{i}{\sqrt{2}\sigma'} \right) e^\gamma \operatorname{erfc}(\sqrt{\gamma}) + \frac{i}{2\pi} \int_{-\infty}^{\infty} Q_{n-1}(x) e^{-\gamma x^2} dx \right] \quad (19)$$

For  $\beta = 1$ , the kernel incorporates a phase shift  $e^{-ix}$  and a scaling factor  $e^1$ . Completing the square in the exponent for the shifted Gaussian  $(-\gamma x^2 - ix)$  leads to:

$$C_n^{(1)} = \mathcal{K}_n \left[ \frac{1}{2} H_n \left( -\frac{i}{\sqrt{2}\sigma'} \right) e^\gamma \operatorname{erfc} \left( \sqrt{\gamma} - \frac{1}{2\sqrt{\gamma}} \right) + \frac{ie}{2\pi} \int_{-\infty}^{\infty} Q_{n-1}(x) e^{-\gamma x^2 - ix} dx \right] \quad (20)$$

The transition from  $\beta = 0$  to  $\beta = 1$  effectively shifts the argument of the error function by  $\Delta = (2\sqrt{\gamma})^{-1}$ .

The analytical results were compared against direct numerical quadrature using a double-exponential integration scheme with a working precision of 30 decimal places. For the parameter set  $\sigma' = 1.2$  and  $\sigma = 2.0$  ( $\gamma = 1/9$ ), the agreement is presented in the tables below.

As demonstrated in Tables 6 and 7, the explicit decomposition method maintains a relative error below  $10^{-25}$ .

Table 6: Comparison of Numerical and Analytical Coefficients for the Lower Bound ( $\beta = 0, \gamma = 1/9$ )

$n$	Numerical Result	Analytical (Explicit)
0	0.4597572626	0.4597572626
1	0.5273259733 <i>i</i>	0.5273259733 <i>i</i>
2	-0.0143676684	-0.0143676684
3	0.3661994074 <i>i</i>	0.3661994074 <i>i</i>

Table 7: Comparison of Numerical and Analytical Coefficients for the Upper Bound ( $\beta = 1, \gamma = 1/9$ )

$n$	Numerical Result	Analytical (Explicit)
0	1.3713254670	1.3713254670
1	-0.8819209173 <i>i</i>	-0.8819209173 <i>i</i>
2	-0.7976665975	-0.7976665975
3	-0.1673816287 <i>i</i>	-0.1673816287 <i>i</i>

### A.3 Proof of Theorem 2

Since the ordinary Hermite functions form a complete orthonormal basis of  $L^2(\mathbb{R})$ , and the dilation  $x = \sigma'y$  is unitary on  $L^2(\mathbb{R})$  after the normalization factor  $1/\sqrt{\sigma'}$ , the squeezed Fock functions also form a complete orthonormal basis of  $L^2(\mathbb{R})$ . Therefore,

$$\lim_{N \rightarrow \infty} \|\psi_\infty - \Pi_{N,r'}^F \psi_\infty\|_2 = 0,$$

proving the existence of a cutoff  $N$  for any prescribed  $\epsilon_s$ .

Under the change of variables  $x = \sigma'y$ , projection onto  $\mathbb{H}_{N,r'}$  is equivalent to ordinary Hermite-function projection of  $F_{r'}(y) = \sqrt{\sigma'}\psi_\infty(\sigma'y)$  onto  $\text{span}\{h_0, \dots, h_{N-1}\}$ . If  $F_{r'} \in \mathcal{S}(\mathbb{R})$ , the Hermite projection estimate of [37, Chapter III], also recalled in [38, Remark 3.10], gives, for every  $s \leq N$ ,

$$\|F_{r'} - \Pi_{N-1}^F F_{r'}\|_2 \leq \frac{\|\mathcal{A}^s F_{r'}\|_2}{\sqrt{N(N-1) \cdots (N-s+1)}}.$$

The Hermite projection error computed for the rescaled function  $F_{r'}(y)$  has the same  $L^2$  norm as the squeezed-Fock projection error in the original variable  $x$ , which proves part (i). For fixed  $s$ , the denominator is  $\Theta(N^{s/2})$ , giving the stated  $\mathcal{O}(N^{-s/2})$  rate.

For part (ii), the stated weighted growth and boundary-integrability assumptions are exactly the hypotheses needed to apply Theorem 3.8(ii) in [38] to the rescaled target  $F_{r'}$  in the strip  $|\text{Im}(y)| < \rho/\sigma'$ . This gives

$$\|F_{r'} - \Pi_{N-1}^F F_{r'}\|_2 \leq C_{r'} \exp\left(-\frac{\rho}{\sigma'} \sqrt{2(N-1)}\right),$$

where  $C_{r'}$  is independent of  $N$ . Returning to the  $x$  variable again preserves the  $L^2$  norm, so the same bound holds for  $\|\psi_\infty - \psi_{N,r'}\|_2$ . Solving the right-hand side for  $\epsilon_s$  gives

$$N = \mathcal{O}\left(e^{2r'} \log^2 \frac{1}{\epsilon_s}\right),$$

completing the proof.

### A.4 Proof of Corollary 1

Let  $\xi \in \mathbb{R}$ . Using the principal branch, write  $1 + i\xi = (1 + \xi^2)^{1/2} e^{i\theta(\xi)}$ ,  $\theta(\xi) = \arctan(\xi) \in (-\frac{\pi}{2}, \frac{\pi}{2})$ . Then

$$\text{Re}[(1 + i\xi)^\beta] = (1 + \xi^2)^{\beta/2} \cos(\beta\theta(\xi)) \geq c_\beta (1 + \xi^2)^{\beta/2},$$

where  $c_\beta = \cos(\beta\pi/2) > 0$  since  $0 < \beta < 1$ . Therefore

$$|g(\xi)| \leq \frac{e^{2\beta}}{2\pi\sqrt{1 + \xi^2}} \exp\left[-c_\beta (1 + \xi^2)^{\beta/2}\right].$$

Repeated differentiation of  $g(\xi)$  only introduces finitely many rational and power factors multiplying the same stretched-exponential term. Since these factors have at most polynomial growth on  $\mathbb{R}$ , for every  $j \geq 0$ ,

$$|\partial_\xi^j g(\xi)| \leq C_j (1 + |\xi|)^{M_j} \exp\left[-c_\beta (1 + \xi^2)^{\beta/2}\right]$$

for some constants  $C_j, M_j > 0$ . Thus, for all nonnegative integers  $m$  and  $j$ ,  $\xi^m \partial_\xi^j g(\xi)$  is bounded on  $\mathbb{R}$ , proving  $g \in \mathcal{S}(\mathbb{R})$ . Multiplication by the normalization constant  $\mathcal{N}$  and the dilation  $F_{r'}(y) = \sqrt{\sigma'} \psi_\infty(\sigma' y)$  preserve the Schwartz class. Theorem 2(i) therefore applies and gives the claimed superalgebraic squeezed-Fock truncation bound.

## A.5 Proof of Theorem 3

For a word  $(G_1, \dots, G_{p+1})$  with  $G_k \in \mathcal{G}$ , define

$$C(G_1, \dots, G_{p+1}) \equiv [G_{p+1}, [G_p, \dots, [G_2, G_1] \dots]].$$

By the commutator-scaling bound for a  $p^{\text{th}}$ -order Suzuki–Trotter formula [39], the simulation error satisfies

$$\left\| e^{-iH_{\text{hyb}}t} - \left[ S_p \left( \frac{t}{n_t} \right) \right]^{n_t} \right\| = \mathcal{O} \left( \frac{t^{p+1}}{n_t^p} \sum_{G_1, \dots, G_{p+1} \in \mathcal{G}} \| [G_{p+1}, [G_p, \dots, [G_2, G_1] \dots]] \| \right).$$

Partition the nested-commutator sum into three disjoint classes:

1. mixed commutators containing at least one  $A_i$  and at least one  $B_j$ ;

$$\Gamma_p^{\text{outer}} \equiv \sum_{\substack{G_1, \dots, G_{p+1} \in \mathcal{G} \\ \text{at least one } G_k \in \{A_i\}_i \\ \text{and at least one } G_k \in \{B_j\}_j}} \| C(G_1, \dots, G_{p+1}) \|$$

2. pure  $A_i$  commutators;

$$\Gamma_p^L \equiv \sum_{i_1, \dots, i_{p+1}} \| C(A_{i_1}, \dots, A_{i_{p+1}}) \|$$

3. pure  $B_j$  commutators.

$$\Gamma_p^H \equiv \sum_{j_1, \dots, j_{p+1}} \| C(B_{j_1}, \dots, B_{j_{p+1}}) \|.$$

For a mixed nested commutator containing exactly  $a$  terms of type  $A_i$  and  $p+1-a$  terms of type  $B_j$ , submultiplicativity of the operator norm implies

$$\| C(G_1, \dots, G_{p+1}) \| \leq \|\hat{x}\|_N^a \| C(R_1, \dots, R_{p+1}) \|,$$

where each  $R_k$  is the corresponding Pauli-level operator drawn from  $\{\alpha_i P_i\}_i \cup \{\beta_j Q_j\}_j$ . Summing over all such mixed words gives  $\Gamma_p^{\text{outer}} \leq \sum_{a=1}^p \|\hat{x}\|_N^a \Gamma_{p,a}^{(L,H)}$ . For the pure  $L$  sector, every summand is of type  $A_i = \alpha_i \hat{x} \otimes P_i$ , so every  $(p+1)$ -fold nested commutator contributes at most  $p+1$  factors of  $\hat{x}$ , yielding  $\Gamma_p^L \leq \|\hat{x}\|_N^{p+1} \Gamma_p^{(L)}$ .

For the pure  $H$  sector, each summand is  $B_j = \beta_j \mathbb{I}_{\text{osc}} \otimes Q_j$ , so no oscillator factor appears, and  $\Gamma_p^H = \Gamma_p^{(H)}$ . Combining these contributions gives

$$\left\| e^{-iH_{\text{hyb}}t} - \left[ S_p \left( \frac{t}{n_t} \right) \right]^{n_t} \right\| = \mathcal{O} \left[ \frac{t^{p+1}}{n_t^p} \left( \sum_{a=1}^p \|\hat{x}\|_N^a \Gamma_{p,a}^{(L,H)} + \|\hat{x}\|_N^{p+1} \Gamma_p^{(L)} + \Gamma_p^{(H)} \right) \right].$$

To ensure the simulation error is at most  $\epsilon_t$ , it is sufficient that

$$\frac{t^{p+1}}{n_t^p} \left( \sum_{a=1}^p \|\hat{x}\|_N^a \Gamma_{p,a}^{(L,H)} + \|\hat{x}\|_N^{p+1} \Gamma_p^{(L)} + \Gamma_p^{(H)} \right) \leq \epsilon_t.$$

Solving for  $n_t$  gives

$$n_t = \mathcal{O} \left[ t^{1+1/p} \left( \frac{\sum_{a=1}^p \|\hat{x}\|_N^a \Gamma_{p,a}^{(L,H)} + \|\hat{x}\|_N^{p+1} \Gamma_p^{(L)} + \Gamma_p^{(H)}}{\epsilon_t} \right)^{1/p} \right],$$

which proves the Trotter-step scaling.

For gate complexity, each Pauli exponential of weight  $w(P_i)$  or  $w(Q_j)$  requires  $\mathcal{O}(2 \max(w-1, 0))$  entangling gates. Since each Trotter step contains  $m_p$  Suzuki layers, the CNOT count scales as

$$N_{\text{CNOT}} = \mathcal{O} \left( 2n_t m_p \left[ \sum_{i=1}^{N_L} \max(w(P_i) - 1, 0) + \sum_{j=1}^{N_H} \max(w(Q_j) - 1, 0) \right] \right).$$

Finally, each  $L$ -sector term requires one hybrid oscillator-qubit interaction per Suzuki layer, implying  $N_{\text{hyb}} = \mathcal{O}(n_t m_p N_L)$ . Thus the theorem follows.

## A.6 Formalism for Inhomogeneous Time-Independent Solution

Let us consider the case when  $A(t) := A = L + iH$  and  $b(t) := b$  and  $b \neq 0$  for all  $t$  and normalized. Starting from Eq. (6) and introducing the elapsed time  $\tau := t - s$ , the inhomogeneous contribution becomes

$$\begin{aligned} u_{\text{inh}}(t) &:= \int_0^t e^{-A(t-s)} b \, ds = \int_0^t e^{-A\tau} b \, d\tau = \int_0^t \int_{\mathbb{R}} g(k) e^{-i\tau(kL+H)} b \, dk \, d\tau \\ &= \int_{\mathbb{R}} \int_{\mathbb{R}} g(k) \mathbb{1}_{[0,t]}(\tau) e^{-i\tau(kL+H)} b \, dk \, d\tau \end{aligned} \quad (21)$$

To embed Eq. (21) into a hybrid oscillator-qubit system, let

$$\mathbb{H}_K = L^2(\mathbb{R}), \quad \mathbb{H}_\tau = L^2(\mathbb{R}), \quad \mathbb{H}_q = \mathbb{C}^D,$$

where the first oscillator encodes the LCHS variable  $k$ , the second oscillator encodes the elapsed time  $\tau$ , and the qubit register stores the source vector  $b$ . In the generalized eigenbases  $\{|k\rangle\}_{k \in \mathbb{R}}$  and  $\{|\tau\rangle\}_{\tau \in \mathbb{R}}$ , define

$$\hat{k} = \int_{\mathbb{R}} k |k\rangle \langle k| \, dk, \quad \hat{\tau} = \int_{\mathbb{R}} \tau |\tau\rangle \langle \tau| \, d\tau.$$

Choose oscillator preparation and postselection states

$$\begin{aligned} |\psi_K\rangle &= \int_{\mathbb{R}} \psi_K(k) |k\rangle \, dk, & \langle \phi_K| &= \int_{\mathbb{R}} \phi_K^*(k) \langle k| \, dk, \\ |\psi_\tau^{(t)}\rangle &= \int_{\mathbb{R}} \psi_\tau^{(t)}(\tau) |\tau\rangle \, d\tau, & \langle \phi_\tau^{(t)}| &= \int_{\mathbb{R}} \phi_\tau^{(t)*}(\tau) \langle \tau| \, d\tau, \end{aligned}$$

such that

$$\phi_K^*(k) \psi_K(k) = g(k), \quad \phi_\tau^{(t)*}(\tau) \psi_\tau^{(t)}(\tau) = \mathbb{1}_{[0,t]}(\tau), \quad (22)$$

where  $\mathbb{1}_{[0,t]}$  is the indicator function on the interval  $[0, t]$ . Strictly, Eq. (22) should be understood up to known normalization factors when  $|\psi_K\rangle$ ,  $|\phi_K\rangle$ ,  $|\psi_\tau^{(t)}\rangle$ , and  $|\phi_\tau^{(t)}\rangle$  are required to be physical normalized oscillator states. These scalar factors are tracked classically and absorbed into the overall LCHS normalization.

We further define the joint preparation state and postselection map

$$\begin{aligned} |\Psi_{\text{inh}}(t)\rangle &:= |\psi_K\rangle \otimes |\psi_\tau^{(t)}\rangle \otimes |b\rangle, \\ \langle \Phi_{\text{inh}}(t)| &:= \langle \phi_K| \otimes \langle \phi_\tau^{(t)}| \otimes \mathbb{I}_q. \end{aligned}$$

The corresponding hybrid unitary on  $\mathbb{H}_K \otimes \mathbb{H}_\tau \otimes \mathbb{H}_q$  is

$$W_{\text{inh}} := \exp \left[ -i \left( \hat{k} \otimes \hat{\tau} \otimes L + I_K \otimes \hat{\tau} \otimes H \right) \right].$$

On a finite truncated oscillator Hilbert space, the above expression becomes a well-defined finite-dimensional unitary. Its action is diagonal in the oscillator variables. For any  $|\varphi\rangle \in \mathbb{H}_q$ ,

$$\left( \hat{k} \otimes \hat{\tau} \otimes L + I_K \otimes \hat{\tau} \otimes H \right) |k, \tau\rangle |\varphi\rangle = |k, \tau\rangle \tau(kL + H) |\varphi\rangle,$$

and therefore

$$W_{\text{inh}} = \int_{\mathbb{R}} \int_{\mathbb{R}} |k, \tau\rangle \langle k, \tau| \otimes e^{-i\tau(kL+H)} \, dk \, d\tau.$$

Taking the oscillator partial inner product yields

$$\begin{aligned}
\langle \Phi_{\text{inh}}(t) | W_{\text{inh}} | \Psi_{\text{inh}}(t) \rangle &= \int_{\mathbb{R}} \int_{\mathbb{R}} \phi_K^*(k) \psi_K(k) \phi_{\tau}^{(t)*}(\tau) \psi_{\tau}^{(t)}(\tau) e^{-i\tau(kL+H)} |b\rangle \, dk \, d\tau \\
&= \int_0^t \int_{\mathbb{R}} g(k) e^{-i\tau(kL+H)} |b\rangle \, dk \, d\tau \\
&= |u_{\text{inh}}(t)\rangle.
\end{aligned} \tag{Eq. (22)}$$

However, note that  $\mathbb{1}_{[0,t]}$  is not analytic. A smooth alternative is given by Gaussian mollification. For  $\varrho > 0$ , let  $h_{\varrho}(x) := \frac{1}{\sqrt{\pi}\varrho} e^{-x^2/\varrho^2}$ , and define

$$\begin{aligned}
w_{\varrho,t}(\tau) &:= (\mathbb{1}_{[0,t]} * h_{\varrho})(\tau) \\
&= \int_{\mathbb{R}} \mathbb{1}_{[0,t]}(s) h_{\varrho}(\tau - s) \, ds \\
&= \int_0^t \frac{1}{\sqrt{\pi}\varrho} \exp\left(-\frac{(\tau - s)^2}{\varrho^2}\right) \, ds \\
&= \int_{\tau-t}^{\tau} \frac{1}{\sqrt{\pi}\varrho} \exp\left(-\frac{x^2}{\varrho^2}\right) \, dx && (x = \tau - s) \\
&= \frac{1}{\sqrt{\pi}} \int_{(\tau-t)/\varrho}^{\tau/\varrho} e^{-v^2} \, dv && \left(v = \frac{x}{\varrho}\right) \\
&= \frac{1}{2} \left[ \text{erf}\left(\frac{\tau}{\varrho}\right) - \text{erf}\left(\frac{\tau - t}{\varrho}\right) \right],
\end{aligned}$$

where  $\text{erf}(x) = \frac{2}{\sqrt{\pi}} \int_0^x e^{-y^2} \, dy$  is the error function. Since  $\int_{\mathbb{R}} h_{\varrho}(s) \, ds = 1$ , we have

$$w_{\varrho,t} - \mathbb{1}_{[0,t]} = \int_{\mathbb{R}} h_{\varrho}(s) \left( \mathbb{1}_{[0,t]}(\cdot - s) - \mathbb{1}_{[0,t]}(\cdot) \right) \, ds,$$

and therefore

$$\begin{aligned}
\|w_{\varrho,t} - \mathbb{1}_{[0,t]}\|_{L^1(\mathbb{R})} &\leq \int_{\mathbb{R}} |h_{\varrho}(s)| \|\mathbb{1}_{[0,t]}(\cdot - s) - \mathbb{1}_{[0,t]}(\cdot)\|_{L^1(\mathbb{R})} \, ds \\
&\leq 2 \int_{\mathbb{R}} |s| |h_{\varrho}(s)| \, ds \\
&= \frac{2\varrho}{\sqrt{\pi}}.
\end{aligned}$$

Hence  $w_{\varrho,t}$  is a Gaussian-smoothed approximation of  $\mathbb{1}_{[0,t]}$  as  $\varrho \rightarrow 0$ . If we instead choose

$$\phi_{\tau,\varrho}^{(t)*}(\tau) \psi_{\tau,\varrho}^{(t)}(\tau) = w_{\varrho,t}(\tau),$$

then the corresponding approximation to the inhomogeneous contribution is

$$|u_{\text{inh},\varrho}(t)\rangle = \int_{\mathbb{R}} \int_{\mathbb{R}} g(k) w_{\varrho,t}(\tau) e^{-i\tau(kL+H)} |b\rangle \, dk \, d\tau.$$

Since  $L$  and  $H$  are Hermitian,  $kL + H$  is Hermitian for real  $k$ , which means  $e^{-i\tau(kL+H)}$  is unitary. In this case, we have the approximation error bound

$$\begin{aligned}
\|u_{\text{inh},\varrho}(t) - u_{\text{inh}}(t)\| &\leq \int_{\mathbb{R}} \int_{\mathbb{R}} |g(k)| |w_{\varrho,t}(\tau) - \mathbb{1}_{[0,t]}(\tau)| \|e^{-i\tau(kL+H)} b\| \, d\tau \, dk \\
&= \|b\| \int_{\mathbb{R}} |g(k)| \, dk \int_{\mathbb{R}} |w_{\varrho,t}(\tau) - \mathbb{1}_{[0,t]}(\tau)| \, d\tau \\
&= \|b\| \|g\|_{L^1(\mathbb{R})} \|w_{\varrho,t} - \mathbb{1}_{[0,t]}\|_{L^1(\mathbb{R})} \\
&\leq \frac{2\varrho}{\sqrt{\pi}} \|b\| \|g\|_{L^1(\mathbb{R})}.
\end{aligned}$$

Therefore, the CV-DV realization of the inhomogeneous term is a continuous linear combination of the unitaries  $e^{-i\tau(kL+H)}$  over two oscillator variables: the LCHS kernel variable  $k$  and the elapsed time  $\tau$ . Compared with the homogeneous construction, the additional ingredient is the second oscillator that encodes the time-window weight  $\mathbb{1}_{[0,t]}(\tau)$  or its approximation  $w_{\varrho,t}$ . For a time-dependent source term  $b(s)$ , the fixed qubit input  $|b\rangle$  must be replaced by a source-time entangled state, which introduces an additional source-state preparation oracle in the qubit space.

## A.7 Gate Counts for $n_t$ First-order Trotterization Block in $d$ -dimensional Heat Equation

Consider the Pauli decomposition of  $T_m^{(bc)}$  for 1-dimensional heat equation

$$T_m^{(bc)} = \sum_{\ell=1}^{N_L^{(bc)}(m)} c_\ell^{(bc)} P_\ell^{(bc)}.$$

For one first-order factor  $e^{-i\theta\hat{x}\otimes P_\ell^{(bc)}}$ , an identity string contributes one hybrid gate, a non-identity string contributes one hybrid gate together with a parity ladder of  $2(w(P_\ell^{(bc)}) - 1)$  CNOTs, and the basis changes contribute 2 one-qubit gates for each  $X$  and 4 for each  $Y$ . Thus, we have

$$\begin{aligned} N_{\text{hyb},1}^{(bc)}(m) &= N_L^{(bc)}(m), \\ N_{\text{CNOT},1}^{(bc)}(m) &= 2 \sum_{\ell=1}^{N_L^{(bc)}(m)} \max(w(P_\ell^{(bc)}) - 1, 0), \\ N_{1q,1}^{(bc)}(m) &= \sum_{\ell=1}^{N_L^{(bc)}(m)} \left[ 2n_X(P_\ell^{(bc)}) + 4n_Y(P_\ell^{(bc)}) \right], \end{aligned}$$

where  $n_X(P)$  and  $n_Y(P)$  denote the numbers of  $X$  and  $Y$  in Pauli string  $P$ . Use the explicit decompositions in Section 5.2.1, we can see the decomposition for the Dirichlet boundary condition contains one identity term and, for each  $c$ , exactly  $2^c$  Pauli strings of weight  $c+1$ . Also, for the one-qubit gates, the  $c=0$  term contributes 2 gates, and each block  $R_c$  with  $c \geq 1$  contributes  $3(c+1)2^c$  basis-change gates.. Therefore, we have

$$\begin{aligned} N_{\text{hyb},1}^{(D)}(m) &= 1 + \sum_{c=0}^{m-1} 2^c = 2^m = M, \\ N_{\text{CNOT},1}^{(D)}(m) &= 2 \sum_{c=0}^{m-1} c 2^c = 2[(m-2)2^m + 2] \\ N_{1q,1}^{(D)}(m) &= 2 + 3 \sum_{c=1}^{m-1} (c+1)2^c = 3(m-1)2^m + 2. \end{aligned}$$

According to the decompositions in Section 5.2.2, for the Neumann boundary condition, the correction contributes  $2^{m-1} - 1$  additional non-identity  $Z$ -type strings and no basis-change gates. Hence, we get

$$\begin{aligned} N_{\text{hyb},1}^{(N)}(m) &= 2^m + 2^{m-1} - 1 = 3 \cdot 2^{m-1} - 1, \\ N_{\text{CNOT},1}^{(N)}(m) &= 2[(m-2)2^m + 2] + 2 \sum_{\substack{S \subseteq \{0, \dots, m-1\} \\ |S| \text{ even}, S \neq \emptyset}} (|S| - 1) = 2^{m-1}(5m - 10) + 6, \\ N_{1q,1}^{(N)}(m) &= 3(m-1)2^m + 2. \end{aligned}$$

Finally, the periodic boundary condition, the final simplified Pauli decomposition keeps the Dirichlet blocks  $R_0, \dots, R_{m-2}$  and replaces the last block by  $2^{m-2}$  weight- $m$  strings. In this case, we obtain,

$$\begin{aligned} N_{\text{hyb},1}^{(P)}(m) &= 1 + \sum_{c=0}^{m-2} 2^c + 2^{m-2} = 3 \cdot 2^{m-2}, \\ N_{\text{CNOT},1}^{(P)}(m) &= 2 \sum_{c=0}^{m-2} c 2^c + 2(m-1)2^{m-2} = 2^{m-1}(3m - 7) + 4, \\ N_{1q,1}^{(P)}(m) &= 2 + 3 \sum_{c=1}^{m-2} (c+1)2^c + \sum_{\substack{S \subseteq \{0, \dots, m-2\} \\ |S| \text{ even}}} (2m + 2|S|) = \begin{cases} 6, & m = 2, \\ 2 + (9m - 13)2^{m-2}, & m \geq 3. \end{cases} \end{aligned}$$

For  $d$  dimensions and  $n_t$  product formula step, the coordinate factors commute, so the total counts are sums of the one-dimensional costs:

$$N_{\text{hyb}}^{(d)} = n_t \sum_{i=1}^d N_{\text{hyb},1}^{(bc_i)}(m_i), \quad N_{\text{CNOT}}^{(d)} = n_t \sum_{i=1}^d N_{\text{CNOT},1}^{(bc_i)}(m_i), \quad N_{1q}^{(d)} = n_t \sum_{i=1}^d N_{1q,1}^{(bc_i)}(m_i).$$

For  $n_t$  product formula step and  $M_i$  grid points for  $i^{\text{th}}$  dimension axis, the gate counts for each boundary conditions are given as a summary in Table 1. The only approximation here is the one-dimensional product formula used within each factor. Since the coordinate factors act on disjoint qubit subregisters they commute exactly, the  $d$ -dimensional split introduces no additional product-formula error. The total error is therefore

$$\epsilon_{\text{heat}}^{(d)} = \sum_{i=1}^d \epsilon_{\text{heat}}^{(i)},$$

where each  $\epsilon_{\text{heat}}^{(i)}$  is estimated by Eq. (15) with the grid spacing  $h_i$  and Laplacian dimension  $m_i$  of axis  $i$ .